学術情報リポジトリ

Nanoscale Probing of Direct Piezoelectric Properties and Vibration Energy Harvesting Application of BiFeO_3 Films

メタデータ	言語: English 出版者: 公開日: 2019-06-25 キーワード (Ja): キーワード (En): 作成者: 苅谷, 健人 メールアドレス: 所属:
URL	https://doi.org/10.24729/00000263

Nanoscale Probing of Direct Piezoelectric Properties and Vibration Energy Harvesting Application of $BiFeO_3$ Films

Kento Kariya

February 2018

Doctoral Thesis at Osaka Prefecture University

Table of Contens

Chapter 1: General introduction

1-1 Research backgrounds 1

1-2 Piezoelectric Films 6

1-3 Objective and Outline of This Thesis 13

References 16

Chapter 2: Piezoelectric Properties of (100) Orientated $BiFeO_3$ Thin Films on $LaNiO_3$

2-1 Introduction 22

2-2 Experiment Procedure 23

2-2-1 Fabrication of $LaNiO_3$ powder target.. 23

2-2-2 Preparation of $LaNiO_3$ and $BiFeO_3$ Thin Films 25

2-2-3 Structural and Electrical Characterization of $LaNiO_3$ and $BiFeO_3$ Films 26

2-2-4 Observation of Domain Structure and Characterization of Converse Piezoelectric Properties using Piezoelectric Force Microscopy 27

2-2-4 Characterization of Direct Piezoelectric Properties using Wafer Bending Technique... 28

2-3 Results and discussion...29

2-3-1 Fundamental Properties of Prepared $LaNiO_3$ Films 29

2-3-2 Piezoelectric Properties of (100) Orientated $BiFeO_3$ Thin Films......... 34

2-3-2 Enhancement of Piezoresponse of (100) Orientated $BiFeO_3$ Films by In-plane Tensile Stress 41

2-4 Conclusions 48

References 49

Chapter 3: Fabrication and Characterization of Electromechanical Transduction Properties of Piezoelectric MEMS Vibrational Energy Harvester Using $BiFeO_3$ Lead-Free Ferroelectric Films

3-1 Introduction 51

3-2 Experiment Procedure 51

3-2-1 Fabrication of Piezoelectric MEMS VEHs with $BiFeO_3$ Films 51

3-2-3 Measurement Set-Up for Characterizing the Electromechanical Transduction Properties 54

3-3 Results and Discussion 56

3-3-1 Output Power Under Ideal Vibration 56

3-3-2 Characterization of the Electromechanical Transduction Properties.. 58

3-3-3 Electromechanical Transduction Properties under Random Oscillations 62

3-4 Conclusions 65

References 67

Chapter 4: Nanoscale Probing of Direct Piezoelectric Response of $BiFeO_3$ Films by Scanning Probe Microscopy

4-1 Introduction 68

4-2 Experiment Procedure 69

4-2-1 Set-up for Nanoscale Characterization of Direct Piezoresponse (DPRM) 69

4-2-2 Detailed Measurement Method and Condition for Accurate DPRM Measurement 71

4-2-3 Finite Element Simulated Electromechanical Properties of DPRM 73

4-2-4 Preparation of Measurement Samples.................................... 74

4-3 Results and discussion 75

4-3-1 Demonstration of DPRM... 75

4-3-2 Observation of Domain Structure Using Direct Piezoelectric Effect ... 79

4-2-3 Quantitative Analysis of Contribution of Domain structure on Direct Piezoresponse of $BiFeO_3$ Films.. 82

4-4 Conclusions 87

References 89

Appendix of Chapter 4

Macroscopic $e_{31,f}$ vs. nanoscopic $d_{33,AFM}$ 90

Determination of domain walls by CPRM 90

DPRM mapping images dependence on compressive force 92
Chapter 5: Summary 94
Acknowledgement 97
Original Articles Regarding This Thesis 98
Other Articles Regarding This Thesis 100

Chapter 1: General introduction

1-1 Research backgrounds

In recent years, the concepts of internet of things (IoT) and machine to machine (M2M) have attracted extensive attentions. Over trillions of "things" and devices will be connected to the internet and distributed into our everyday lives to improve the quality of life by gathering information from human activities. Various types of information such as temperature, humidity, illumination, pressure, motion, and stress need to be gathered by using sensor nodes, which is composed of several sensors, a micro-computer, an RF transmitter, and electrical power sources.

The recent progress of the reduction of power consumption for sensors, microcomputers, and wireless communication has allowed development of sensor nodes to realize IoT and M2M [1]. It is reported that the average electric power of approximately 100 μW is sufficient to operate the sensor nodes under relatively high data-rate [2-4]. Such electric power could be covered by an energy harvesting from the environment [5,6]. The energy harvester is one of the keys to realize battery-less autonomous sensor nodes for IoT and M2M.

In the ambient environment, various energy sources exist: light, mechanical, and thermal, energies. The potential energy densities of these sources have a wide range from $\mu W/cm^2$ to mW/cm^2 [7]. Among them, the energy density of the sunlight is clearly the highest. While the solar cell is a primal candidate for the power source, there are many situations where the sunlight is not available. Power scavenged from thermal energy is also attractive if the necessary thermal gradient is available. Since the

efficiency of thermoelectric generators is regularly low, greater than 10ºC thermal gradient is needed to produce sufficient output power for IoT and M2M. It is, however, difficult to find large thermal gradient in the ambient environment. By comparing them, mechanical vibrations are present in various objects with sufficiently high energy density for the self-powered operation of the sensor nodes. The mechanical energy source can be not only the operating movement of industrial structure and human motion but also flow of fluid. They have the wide range of acceleration from 0.1s-10s m/s^2 and frequency range from 1s-100s Hz [8]. These vibration energies are produced steadily when the human activities are performed, therefore, mechanical vibrations are available in most cases as a quite stable and reliable energy source [9-13].

Vibrational energy harvesters (VEHs) are classified in two categories: the non-resonant and resonant type. For non-resonant type VEHs, force is directly applied to the transducer. Therefore, the non-resonant type VEHs have characteristic of simple structure and the efficiency is simply given by the electromechanical coupling factor (K^2). As the kinetic energy of the vibrating object is proportional to the mass and the inverse of the square of the frequency, the non-resonant type VEHs are suitable for objects with large mass and low vibrational frequencies such as human. It is expected to obtain electrical power above 100μW even if K^2 of the harvester is as low as 1% [14-16]. In contrast, IoT and M2M need to deal with the movement of objects more extensively, which has a frequency region of 10-200 Hz. As the input mechanical energy decreases dramatically in this frequency region, the resonant type VEHs are employed to obtain high conversion efficiency at the resonance [17].

VEHs have several mechanisms to convert mechanical energy into electrical

energy including electromagnetic, inverse magneto-striction, electrostatic, and piezoelectric [18-21]. Their schematic figures and features are summarized in Table. 1.1. Electromagnetic and inverse magneto-striction based VEHs require relatively large device volume (>>1 cm^3) because of the difficulty of the miniaturization of the coil and proportional relationship between the output voltage and the device size [22,23]. However, electrostatic and piezoelectric VEHs typically have large output voltage due to the large output impedance even if the structure is downsized. Since sensor nodes are distributed in various places, compact design and stable performance of the VEHs are hoped. Electrostatic VEHs has elaborate vibrational structure, and they are reported that surface potential decay is severe in a moist environment since the surplus charges of electret are neutralized by the ions in the water [24,25]. Thus, piezoelectric VEHs, which is compatible with microelectromechanical systems (MEMS), are adopted in this thesis [26-32]. To develop practical and high-performance VEHs, it is necessary to comprehensively understand the mechanical and electrical domains, leads to vibrational structure and the material science of piezoelectric films, respectively. In the following sections, the recent progress of the VEHs and development of piezoelectric films are introduced.

Table 1.1: Comparison of VEHs with different transduction mechanism.

Transduction Type	Advantages	Disadvantages
Electromagnetic	･High output current ･Low output impedance	･Difficult to integrate with MEMS fab. process ･Poor performance in micro-scale ･Low output voltage
Inverse magnet strictive	･High efficiency ･Low output impedance	･Difficult to integrate with MEMS fab. process ･Anharmonic output signal
Electrostatic	･High output voltage ･Easy to miniaturize	･Mechanical constraints needed ･Elaborated design ･High output impedance ･Low output current
Piezoelectric	･High output voltage ･easy design ･Compatible with MEMS	･Poor E-M coupling of thin-films ･High impedance

Most of the reported MEMS VEHs use a unimorph-typed cantilever with a proof mass at the free end. The structure is simple and easy to design, fabricate, and forecasts the electromechanical properties. However, the bandwidth is typically narrow owing to the high quality factor. Since high quality factor is needed to obtain the large electromechanical output, there is a trade-off between the output power and the bandwidth. In some applications where the frequency of vibrational source fluctuates, this structure is impractical. To overcome the limitation, some modified vibrational

structures are proposed.

Hajati *et al*. developed a doubly-clamped non-linear resonator at MEMS scale with two fixed ends and a proof-mass in the middle, which achieved an ultra-wide bandwidth of >20 % of peak frequency and large output power of 45 μW [33]. The vibrational structure is designed to produce the stretching strain at large deformation (>thickness of the beam), which shows a nonlinear stiffness. Since it can act as negative feedback toward the change of resonance frequency, the wider frequency range and large output property could be obtained.

Recently, Xu *et al*. proposed the Bi-stable nonlinear MEMS resonators with buckled beam structure, employing residual stress in micro-fabricated thin films [34]. The Bi-stable oscillator has double-well restoring force potential [35]. When the large amplitude is applied to the oscillator, the potential energy exceeds the barrier height of well. The oscillator, therefore, exhibits significantly large electromechanical response with wide bandwidth at relatively low-frequency range. Although the output power of MEMS-scale prototype hasn't been characterized yet, the bi-stable response could be obtained at the macro-scale prototype and further progress are expected.

These vibrational structures can be promising one if they are easy to be fabricated using the MEMS process. However, since the internal stress in the structure is controlled precisely to realize the non-linear stiffness or bi-stable behavior, it needs special manufacturing ability and costly and is impractical. Thus, although the cantilever-type VEHs exhibit high quality factor, from the aspects of mass production, it is one of the most compatible structure with MEMS process.

Renaud *et al*. developed a model for VEHs and the cantilever-type VEHs with

high quality factor and high electromechanical properties exhibit two power peaks at different resonant frequency [36]. This means MEMS cantilever-type VEHs with high performance piezoelectric films can broad the bandwidth by the improving the properties of piezoelectric films. This behavior is originated from fundamental resonant and anti-resonant characteristics of piezoelectric transducers and is quite challenging topics from the aspects of material science of piezoelectric thin films. Therefore, in this thesis, cantilever-type vibrational structure is applied as a vibrational structure.

1-2 Piezoelectric Films

Piezoelectricity is a phenomenon, where mechanical energy is directly converted into electrical energy and vice versa, and has been used in various applications such as sensors, actuators, and transducers. The piezoelectric materials, which have crystal structure without centrosymmetry, can generate the charge or mechanical stress when a strain or an electric field is applied, respectively. These are called as direct and converse piezoelectric effect, respectively.

$Pb(Zr,Ti)O_3$ (PZT) is the most studied and used ferroelectric thin films in the field of piezoelectric MEMS. PZT exhibits electromechanical coupling coefficient of piezoelectric film (k_{31}^2) as high as 10 % owing to the large $e_{31,f}$ [37,38]. Higher k_{31}^2 (≈20 %) was reported on Pb-based relaxor thin films [39]. While Pb-based ferroelectric films have outstanding electromechanical properties, the lead containing is the serious drawback for IoT applications.

Piezoelectric VEHs using AlN thin films have also been reported by many groups [40-42]. Microgen Systems have reported the output power of 100μW

(100μW·mm^{-2}·G^{-2}) at a frequency of 120Hz and an acceleration of 0.1 G. Although the $e_{31,f}$ of AlN films is much smaller than PZT, a relatively large k_{31}^2 (≈2.3 %) is obtained because of the small ε_{33} [43]. Moreover, it is recently reported that the doping of Sc into AlN film enhance the k_{31}^2 (≈ 3.5%) by the structural phase competition between the parent wurtzite and hexagonal phase of the alloy [44,45].

(K,Na)NbO_3 (KNN)-based ceramics are known as the promising lead-free piezoelectric material [46]. Thus KNN thin films has also been studied. Kanno *et al.* demonstrated the piezoelectric MEMS VEH with a (100)-orientated KNN thin film and reported the electromechanical properties. The k_{31}^2 estimated from the power generation properties is about 4.2 %, which is larger than AlN [47].

(Bi,K)TiO_3 based system has also attracted much attentions. The k_{31}^2 of (100) epitaxial (Bi,Na)TiO_3-(Bi,K)TiO_3-$BaTiO_3$ (BNT-BKT-BT) was reported to be 0.75 % [48]. Although the k_{31}^2 is much lower than that of other films, the BNT-BKT-BT ceramics exhibit large electromechanical properties (k_{33}^2=56 %) [49]. Further progress in the enhancement of k_{31}^2 can be expected.

The k_{31}^2 of various piezoelectric films are summarized in Fig. 1.5. Although the developments of piezoelectric films have been activated, the specific application is not defined and the films are characterized using various methods as described below. Therefore, the designing principle of piezoelectric films for VEHs is not established. The k_{31}^2 comparable to PZT haven't also been reported yet in lead-free thin film.

This study focuses on $BiFeO_3$ films as lead-free ferroelectric thin films for MEMS VEHs owing to their high Curie temperature (T_c=850 ºC) and high remnant polarization (P_r=100 μC/cm^2) [50]. The large polarization of $BiFeO_3$ originated from the

hybridization between the long-pair 6s orbital in the A site (Bi^{3+}) and the 2p orbital of oxygen that is the same as that between Pb-O [51]. Furthermore, $BiFeO_3$ displays G-type antiferromagnetic ordering at room temperature. Owing to the rhombohedral symmetry, $BiFeO_3$ has eight distinct domain variants along the <111> directions and three distinct domain walls, which are the 71º, 109º, and 180º domain walls, along the {100} and {101} plane at the boundary of each domain [52].

It has been reported that the domain-engineered (100) epitaxial $BiFeO_3$ films has a large k_{31}^2 (~10.2 %), comparable to the PZT films [53-55]. From above described characteristics, this material can have a potential to compare to or surpass the electromechanical properties of PZT films.

The motivation of this thesis is to investigate how to design the lead free piezoelectric films with large k_{31}^2, comparable with PZT. Since the piezoelectric response of ferroelectric films is quite complex, the research is focused on the application of VEHs. Piezoresponse of ferroelectric films is originated from nanoscopic dipole domain structure. According to the application, the required performance of piezoelectric films should also be different. Thus, this research is progressed in connecting the structural design of VEHs with the investigation of piezoelectric properties at nanoscopic region.

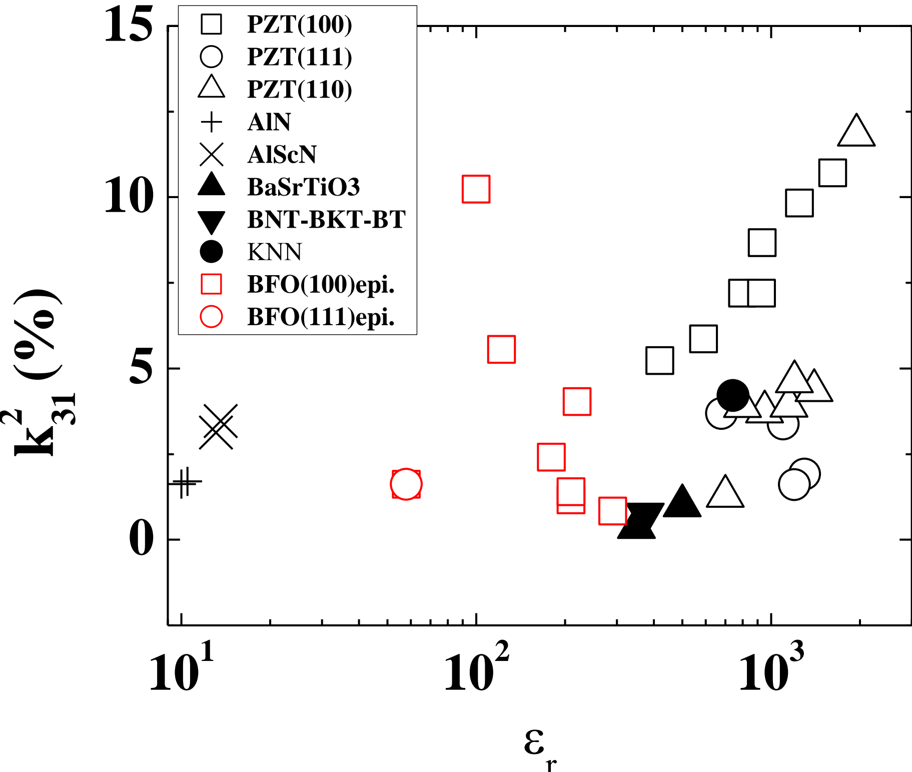

Fig. 1.1: Reported electromechanical coupling coefficient of thin films (k_{31}^2) dependent on the relative permittivity.

Ferroelectric materials have significantly larger piezoelectricity than pure piezoelectric materials owing to spontaneous polarization. Moreover, since the ferroelectric materials have unique and complex domain structures, the piezoresponse consists of two major contributions.

As intrinsic piezoresponse, the lattice deformation and the domain-engineered configuration are well known. The former is a fundamental mechanism of piezoresponse. The latter is the contribution via the electrical dipole rotation by the crystallographic anisotropy of the ferroelectrics. Park *et al.* reported that the piezoelectric coefficient of the domain-engineered (100) $Pb(Zn_{1/3}Nb_{2/3})O_3$-$PbTiO_3$ single crystal was 25 times larger than the (111) single crystal and the

domain-engineered configuration was effective in enhancing the piezoresponse significantly [56].

The piezoresponse, which arises at the vicinity of the domain walls, can also contain the domain wall motion and stationary (or iced) domain wall contribution in addition to the intrinsic contribution. The first originated form dipoles switching without volume change in their unit cells [57]. The second is considered as the local-phase transition between stable and metastable phases which occurs without domain wall motion [58]. Especially, recent studies indicate that the stationary domain wall is expected to be an effective method to enhance the piezoelectric properties [58-60].

In Pb-based films, two effects: domain-engineering and morphotropic phase boundary (MPB) as the origins of the large k_{31}^2 are reported. The (100) and (110) films exhibit quite a large k_{31}^2 (10%-20%) owing to the dipole rotation, in contrast to the (111) film (k_{31}^2 ≈3.4 %) [38,61]. A large k_{31}^2 is also observed at the MPB, a phase boundary region between the tetragonal and rhombohedral structures. From the experimental results of bulk ceramics, at the vicinity of MPB, it is known that polarization rotation is activated owing to an intermediate monoclinic phase between the rhombohedral and the tetragonal phase [62,63].

Hence the piezoresponse of the ferroelectric materials contains various contributions from the intrinsic and extrinsic responses. To fabricate piezoelectric films with large electromechanical properties, it is imperative to understand the magnitude of each contribution to construct the designing principle.

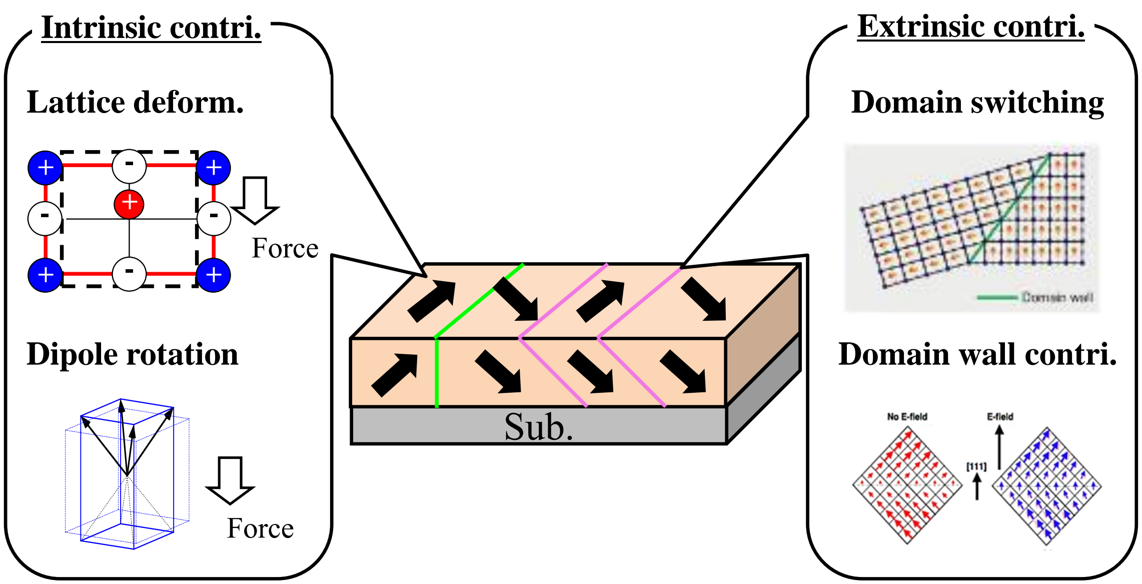

Fig. 1.2: Intrinsic and extrinsic contribution to piezoresponse.

To characterize the piezoresponse of ferroelectric films, various characterization methods have been developed. The principle of the measurement is based on 2 types: the direct piezoelectric effect or converse piezoelectric effect. The representative setup is summarized in Fig. 1.4.

Dubois *et al*. reported a bending method for determining the effective transverse piezoelectric stress coefficient ($e_{31,f}$) of thin films in macroscopic regions using the direct piezoelectric effect [64]. This method has been improved to a four-point bending measurement, which can measure not only $e_{31,f}$, but also the effective transverse piezoelectric strain coefficient ($d_{33,f}$) of thin films in macroscopic regions [65]. In these methods, a piezoelectric film is bent to apply a stress and then the electrical charge induced by the direct piezoelectric effect is collected.

Chun et al. developed a characterization method to measure $e_{31,f}$ from

converse piezoelectric by measuring the electrical-field induced displacement of the cantilever with piezoelectric film [66]. Since it is easy to estimate $e_{31,f}$, many researchers have used it recently.

Piezoelectric force microscopy (PFM) is also widely utilized as the characterization method for piezoelectricity, because it is useful in observing the domain structure and the nanoscopic $d_{33,f}$ from the converse piezoelectric effect [67]. In PFM, a conductive cantilever is attached onto a film and an electric filed is applied to the film. The converse piezoresponse is detected by the motion of the cantilever motion using a photo detector. Since the out-of-plane and in-plane signal can be detected individually, domain structure can be visualized by mixing these signals.

Recently, some interesting experimental results have been reported. The effective transverse piezoelectric coefficients $|e_{31,f}|$ of $Pb(Zr,Ti)O_3$ film determined by the direct and converse piezoelectric effect does not coincide [68]. This results is not observed in AlN-type piezoelectric thin films [69]. Moreover, the quantitativity of PFM has been argued because some contributions such as the electrostrictive and charging effects is superimposed on the piezoelectric effect [70,71].

These problems prevent the effective development of the piezoelectric films for the application of MEMS devices owing to the scientific knowledges are not connected.

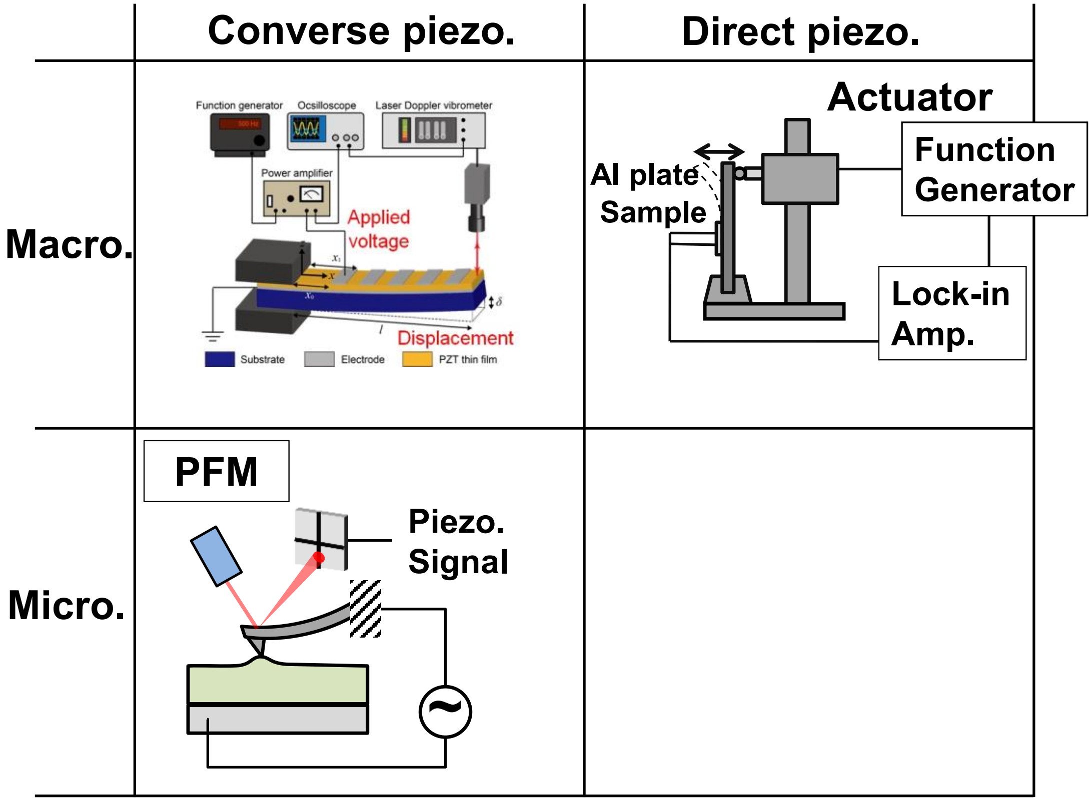

Fig. 1.3: Established setup for characterizing piezoresponse.

1-3 Objective and Outline of This Thesis

The objective of this thesis is to develop a lead-free piezoelectric thin film with large k_{31}^2, comparable to PZT films, for VEHs. Comprehensive studies on electromechanical properties, including macroscopic and nanoscopic region, of piezoelectric thin films and VEHs were conducted.

This thesis consists of 5 chapters.

In chapter 2, the growth and piezoelectric properties of (100) oriented $BiFeO_3$ films on the Si substrate were investigated. To control the orientation of the $BiFeO_3$ films on the Si substrate, The $LaNiO_3$ is introduced as a seed layer on the Si substrate. The $LaNiO_3$ thin films are prepared by sputtering using a homemade powder target. The

$BiFeO_3$ films are also crystalized on the prepared $LaNiO_3/SiO_2/Si$ by the sol-gel method. From the results of X-ray diffraction (XRD) analysis, the prepared $LaNiO_3$ and $BiFeO_3$ thin films grew with the (100) texture orientation. The ferroelectric properties, microscopic converse piezoelectric response, and macroscopic direct piezoresponse of (100)-oriented $BiFeO_3$ thin films were investigated. It was found that the enhancement of direct piezoresponse by the tensile stress applied to the $BiFeO_3$ films from $LaNiO_3$ bottom electrodes.

In chapter 3, the electromechanical properties of MEMS VEHs using the $BiFeO_3$ films are characterized. Unimorph cantilever-type VEHs are fabricated using Si micro-electrical system technologies. The electrical and mechanical performance of VEHs with $BiFeO_3$ films are measured by the voltage, generated by the electrical charge consumed at the applied load resistance, and the tip-displacement using lock-in-amplifiers and the leaser-displacement meter. From the energy balance derived from the Duffing equation and the Kirchhoff equation, the accurate electromechanical coupling coefficients of the VEHs are also analyzed. By comparing the results of numerical calculations with experimental results, the efficiency of the developed VEHs is discussed. Moreover, the electromechanical properties of VEHs under random oscillations are characterized. Environmental vibrations include random oscillations of different frequencies and amplitudes. The contributions of spurious components to the fabricated VEHs under random oscillation are analyzed. From the experimental and calculation results, the required performance of piezoelectric films for VEHs was concluded as the $k_{31}^2 \approx 10\%$.

In chapter 4, the technique to observe the local direct piezoresponse of thin films is proposed, called as direct piezoresponse microscopy (DPRM). It is needed to enhance the electromechanical coupling property of the $BiFeO_3$ film for achieving maximum performance of VEHs. Nanoscopic characterization of direct piezoresponse can be one of the keys to clarify the required factor to enhance the property. To investigate the microscopic direct piezoresponse, direct piezoresponse microscopy (DPRM) is developed. In DPRM, the local mechanical compressive force from a conductive cantilever, fixed at a constant deflection on the sample, is applied to a sample by vibrating the sample stage. The measurement principle and the resolution of DPRM are discussed. Furthermore, the contributions of the domain structures to the direct piezoresponse are analyzed by DPRM. (111) $BiFeO_3$ film with single-domain structure and (100) $BiFeO_3$ film with three variant domain walls are used. Since the compressive mechanical force applied by DPRM is parallel to the dipole of the (111) film, the induced piezoresponse should be due to the intrinsic contribution. However, the direct piezoresponse of the (100) film can superimpose the extrinsic contribution to the intrinsic contribution because the dipole direction is not parallel to the direction of applied force and contains domain walls. By comparing these responses between the macroscopic and microscopic regions, specific domain walls formed inside $BiFeO_3$ films contributed to the piezoresponse significantly and it was found that the design of lead-free ferroelectric films utilizing extrinsic contribution is needed to achieve the large k_{31}^2, comparable with PZT.

In chapter 5, the results and discussions throughout my doctoral thesis were summarized.

References

[1] R.J.M. Vullers, R. van Schaijk, I. Doms, C. Van Hoof, R. Mertens, Solid-State Electronics **53,** 684 (2009)

[2] Cook BW, Lanzisera S, Pister KSJ. SoC issues for RF smart dust. Proc IEEE 2006;94:1177–96.

[3] Mitcheson PD, Yeatman EM, Rao GK, Holmes AS, Green TC. Energy harvesting from human and machine motion for wireless electronic devices. Proc IEEE 2008;96:1457–86.

[4] Tom Torfs, Vladimir Leonov, Chris Van Hoof. Bert gyselinckx body-heat powered autonomous pulse oximeter. In: 5th IEEE conference on sensors; 2006. p. 427–30

[5] IEA World Energy Outlook (2008).

[6] Energy Harvesting report, November 2012, Yole Development.

[7] M. Matak and P. Solek, American Journal of Mechanical Engineering, **1,** 7 438 (2013).

[8] M. Amin Karami and Daniel J. Inman, Appl. Phys. Lett. **100**, 042901 (2012).

[9] S. Roundy, Paul K. Wright, and J. Rabaey, Com. Comm. **26,** 1131 (2003).

10] Y. Suzuki, IEEJ Trans **6,** 101 (2011).

[11] P. D. Mitcheson, E. M. Yeatman, G. K. Rao, A. S. Holmes, Proc. IEEE **96,** 9 (2008).

[12] S. F. Ali, M. I. Friswell and S. Adhikari, Journal of Intelligent Material Systems and Structures **22,** 16 1929 (2011).

[13] Eskild R. Westby and Einar Halvorsen, Mechatoronics, IEEE/ ASME Trans. **17,** 5

2012.

[14] J. Kymissis, C. Kendall, J. Paradiso, and N. Gershenfeld, Second IEEE Int'l Conf. Wearable Computing, 132 (1998).

[15] N. S. Shenck and J. A. Paradiso, 2001 IEEE Micro **21,** 30 (2001).

[16] J. Zhao and Z. You, *Sensors* **14,** 12497 (2014).

[17] S. Priya, H. C. Song, Y. Zhou, R. Varghese, A. Chopra, S. G. Kim, I. Kanno, L. Wu, D. S. Ha, J. Ryu, and R. G. Polcawich, A Review on Piezoelectric Energy Harvesting (2017).

[18] M. EI-hami, P. Glynne-Jones, N. M. White, M. Hill, S. Beeby, E. James, A. D. Brown, and J. N. Ross: Sens. Actuators A **92,** 335 (2001).

[19] D. Hoffmann, B. Folkmer, and Y. Manoli: Proc. Power MEMS 2008+microEMS 2008, 2008, p. 15.

[20] J. -Q. Liu, H. -B. Fang, Z. -Y. Xu, X. -H. Mao, X. -C. Shen, D. Chen, H. Liao, and B. -C. Cai: Microelectron. J. **37,** 1280 (2006).

[21] T. Ueno, J. Appl. Phys. **117,** 17A740 (2015).

[22] A. Marin and S. Priya, SPIE Smart Structures and Materials Nondestructive Evaluation and Health Monitoring, 83411L-L–11 (2012).

[23] Bono, D. C., A. Sliski, J. Huang, and R. C. O, US Patent 7,569,952.

[24] Sessler, G. M, Journal of Electrostatics **51,** 137 (2001).

[25] A. Sorimachi, H. Takahashi, and S. Tokonami, Radiation Measurements **44,** 111 (2009).

[26] S. Roundy, P. K. Wright, Smart Mater. Struct. **13**, 1131 (2004).

[27] K. Morimoto, I. Kanno, K. Wasa, and H. Kotera, Sens. Actuators A **163**, 428

(2010).

[28] P. Muralt, M. Marzencki, B. Belgacem, F. Calame, and S. Basrour, Procedia Chem. **1**, 1191 (2009).

[29] H. Durou, G. A. Ardila-Rodriguez, A. Ramond, X. Dollat, C. Rossi, and D. Esteve, Power MEMS, 2010, p. 27.

[30] M. Renaud, K. Karakaya, T. Sterken, P. Fiorini, C. Van Hoof, and R. Puers, Sens. Actuators A **145,** 380 (2008).

[31] A. Massaro, S. D. Guido, I. Ingrosso, R. Cingolani, M. D. Vittorio, M. Cori, A. Bertacchini, L. Larcher, and A. Passaseo, Appl. Phys. Let. **98,** 053502 (2011).

[32] R. Elfrink, T. M. Kamel, M. Goedbloed, S. Matova, D. Hohlfeld, R. van Schaijk, and R. Vullers, Proc. Power MEMS 2008+microEMS2008, p. 249.

[33] A. Hajati and S.-G. Kim, Appl. Phys. Lett. **99,** 083105 (2011).

[34] R. Xu and S. Kim, Power MEMS 012013 (2015).

[35] R. L. Harne and K. W. Wang, Smart Mater. Struct. **22,** 023001 (2013).

[36] M. Renaud, K. Karakaya, T. Sterken, P. Fiorini, C. Van Hoof, R. Puers, Sens. Act. A **145,** 380 (2008).

[37] C. B. Yeager1, Y. Ehara, N. Oshima, H. Funakubo, and S. T. McKinstry, J. Appl. Phys. **116,** 104907 (2014).

[38] X. Wan, E. P. Houwman, R. Steenwelle, R. van Schaijk, M. D. Nguyen, M. Dekkers, and G. Rijnders, Appl. Phys. Lett. **104,** 092902 (2014).

[39] S. H. Baek, J. Park, D. M. Kim, V. A. Aksyuk, R. R. Das, S. D. Bu, D. A. Felker, J. Lettieri, V. Vaithyanathan, S. S. N. Bharadwaja, N. Bassiri-Gharb, Y. B. Chen, H. P. Sun, C. M. Folkman, H. W. Jang, D. J. Kreft, S. K. Streiffer, R. Ramesh, X. Q. Pan, S.

Trolier-McKinstry, D. G. Schlom, M. S. Rzchowski, R. H. Blick, and C. B. Eom, Science **334,** 958 (2011).

[40] R. Elfrink, T. M. Kamel, M. Goedbloed, S. Matova, D. Hohlfeld, R. van Schaijk, and R. Vullers, Journal of Micromechanics and Microengineering **19,** (9):094005 (2009).

[41] M. Defosseux , M. Allain , P. Ivaldi , E. Defay , S. Basrour , Proc. of 16th International Conference on Solid-StateSensors, Actuators and Microsystems 1859 (2011).

[42]. M. Marzencki , Y. Ammar , S. Basrour , Proc. Int. Conf. on Solid-State Sensors, Actuators, and Microsystems, Lyon 887 (2007).

[43] S. Trolier-Mckinstry and P. Muralt, J. Electroceram. **12**, 7 (2004).

[44] R. Matloub, M. Hadad, A. Mazzalai, N. Chidambaram, G. Moulard, C. S. Sandu, Th . Metzger, and P. Muralt, Appl. Phys. Lett. **102,** 152903 (2013).

[45] F. Tasnadi, B. Alling, C. Hoglund, G. Wingqvist, J. Birch, L. Hultman, and I. A. Abrikosov, Phys. Rev. Lett. **104,** 137601 (2010).

[46] Ahn, C.-W., C.-H. Choi, H.-Y. Park, S. Nahm, and S. Priya. J Mater Sci. **43,** 6784 (2008).

[47] I. Kanno, T. Ichidab, K. Adachia, H. Koterab, K. Shibatac, T. Mishimac, Sens. Act. A **179,** 132 (2012).

[48] M. Abazari, A. Safari, S. S. N. Bharadwaja, and S. Trolier-McKinstry, Appl. Physis. Lett. **96**, 082903 (2010).

[49] Y. Hiruma, H. Nagata, and T. Takenaka, Jpn. J. Appl. Phys., Part 1 **45,** 7409 (2006).

[50] C. Wang, M. Takahashi, H. Fujino, X. Zhao, E. Kume, T. Horiuchi, and S. Sakai, J.

Appl. Phys. **99,** 054104 (2006).

[51] F. Kubel and H. Schmid, Acta Cryst. **B46,** 698 (1990).

[52] J. Wang, J. B. Neaton, H. Zheng, V. Nagarajan, S. B. Ogale, B. Liu, D. Viehland, V. Vaithyanathan, [] D. G. Schlom, M. Wuttig, and R. Ramesh, Science **229,** 1719 (2003).

[53] K. Ujimoto, T. Yoshimura, A. Ashida, and N. Fujimura Appl. Phys. Lett. **100,** 102901 (2012).

[54] T. Yoshimura1, K. Ujimoto, Y. Kawahara1, K. Wakazono, K. Kariya1, N. Fujimura1, and S. Murakami, Jpn. J. Appl. Phys. **52,** 09KA03 (2013).

[55] K. Ujimoto, Ph. D. Dissertation in Osaka Prefecture University.

[56] Seung-Eek Park and Thomas R. Shrout ,J. Appl. Phys. **82**, 4 (1997).

[57] N. B. Gharb, I. Fujii, E. Hong, S. Trolier-McKinstry, D. V. Taylor, and D. Damjanovic, J. Electroceram. **19,** 47 (2007).

[58] W. F. Rao and Y. U. Wang, Appl. Phys. Lett. **90**, 041915 (2007).

[59] S. Wada, K. Yako, H. Kakemoto, T. Tsurumi, and T. Kiguchi, J. Appl. Phys. **98**, 014109 (2005).

[60] R. Xu, J. Karthik, A. R. Damodaran, and L. W. Martin, nat. Nat. Commun. **5**, 3120 (2014).

[61] N. Ledermann, P. Muralt, J. Baborowski, S. Gentil, K. Mukati, M. Cantoni, A. Seifert, and N. Setter, Sens. Act. A **105,** 162–170 (2003).

[62] M. Iwata and Y. Ishibashi, Jpn. J. Appl. Phys. Part 1 **44**, 3095 (2005).

[63] D. Damjanovic, Appl. Phys. Lett. **97**, 062906 (2010).

[64] M.-A. Dubois and P. Muralt, Sens. Act. A, Phys,. 77, 2 106 (1999).

[65] K. Prume, P. Muralt, F. Calame, T. Schmitz-Kempen, and S. Tiedke, IEEE Trans.

Ultrason., Ferroelectr., Freq. Control,. **54,** 1 8 (2007)..

[66] D.-M. Chun, M. Sato, and I. Kanno, J. Appl. Phys., **113,** 4 044111 (2013).

[67] Sergei V. Kalinin and Dawn A. Bonnell, Phys. Rev. B, **65**, 125408 (2002).

[68]Y. Tsujiura, S. Kawabe, F. Kurokawa, H. Hida, and I. Kanno, Jpn. J. Appl. Phys. **54,** 10NA04 (2015).

[69] A. Mazzalai, D. Balma, N. Chidambaram, R. Matloub, and P. Muralt, Journal of Microelectromechanical Systems, **24**, 4 (2015).

[70] R. K. Vasudevan, S. Zhang, J. Ding, M. B. Okatan, S. J. Sergei, V. Kalinin, and N. Bassiri-Gharb, Appl. Phys. Lett. **106**, 222901 (2015).

[71] N. Balke, P. Maksymovych, S. Jesse, Ivan I. Kravchenko, Qian Li, and Sergei V. Kalinin, ACS Nano **8**, 10229 (2014).

Chapter 2: Piezoelectric Properties of (100) Orientated $BiFeO_3$ Thin Films on $LaNiO_3$

2-1 Introduction

As described in Chapter 1, since the engineered-domain configuration can enhance the piezoelectric properties of the $BiFeO_3$ epitaxial films, it can also be expected that the Piezoelectric vibrational energy harvesters (VEHs) using the (100) oriented $BiFeO_3$ films should have better performance than that using polycrystalline $BiFeO_3$ films [1-3].

In this chapter, the control of the growth orientation of $BiFeO_3$ films toward (100) direction on Si substrate are addressed. Since the polycrystalline $BiFeO_3$ films on metal electrode such as Pt, which is commonly used in MEMS devices, are obtained, $LaNiO_3$ is employed as the bottom electrode and seed layer of $BiFeO_3$ films. $LaNiO_3$ is a perovskite-type metal oxide with pseudocubic structure. It is known that $LaNiO_3$ shows preferential (100) orientation on Si and other substrates [4,5]. The lattice parameter is 3.84 Å [6,7], which matches well with the perovskite-type ferroelectric thin films [4,8,9]. The lattice misfit between $BiFeO_3$ and $LaNiO_3$ is -3.1 % [10], which is slightly larger than that between $BiFeO_3$ and $SrRuO_3$.

Here, the growth and piezoelectric properties of (100) orientated $BiFeO_3$ films on Si substrate are investigated. The piezoelectric properties are manly characterized using 3-1 mode, which is utilized in VEHs, and the electromechanical coupling coefficient (k_{31}^2) is calculated using eq. (2.1)

$$k_{31}^2 = \frac{(1-v)^2}{E}\frac{e_{31,f}^2}{\varepsilon_0\varepsilon_r} \quad (2.1)$$

where $e_{31,f}$ is transverse piezoelectric stress coefficient of piezoelectric films, v Poisson's ratio; E Young's modulus of the cantilever; and ε_0 and ε_r are the permittivity of the vacuum and the relative permittivity of the piezoelectric film respectively [11]. For the calculation of k_{31}^2, the E and v of $BiFeO_3$films were assumed as 100 GPa and 0.3, respectively.

2-2 Experiment Procedure

2-2-1 Fabrication of $LaNiO_3$ powder target

$LaNiO_3$ thin films were deposited on the SiO_2/(100)Si substrate by rf magnetron sputtering. To fabricate a $LaNiO_3$ powder target, optimal calcination temperature of $LaNiO_3$ powder was investigated. Stoichiometric amounts of La_2O_3 and NiO powder, which both have 99.99% purity, were weighted and mixed using ball mill for 24 h. Then the powder was calcined at 850-1100 ºC for 3 hours. From the result of XRD profiles of prepared powders shown in Fig. 2.1, it is found that several co-oxide phases, including $LaNiO_3$ (850 ºC), $LaNiO_3$ and $La_4Ni_3O_{10}$, (900-1000 ºC) and $LaNiO_3$, $La_4Ni_3O_{10}$, and $La_3Ni_2O_7$ (>1000 ºC), could be obtained. The calcination temperature of 850 ºC, therefore, was used to prepare $LaNiO_3$ target. Since the reaction between La_2O_3 and NiO was not active, the calcination for 25 h is separated to three times (first: 5h, second: 10h, third: 10h) to accelerate them. The powder was also treated by ball mill after each calcination. The XRD profiles of $LaNiO_3$ powders obtained by the each calcination are shown in Fig. 2.2(a). Although no-reacted NiO still remains in the

powder prepared by third calcination, $LaNiO_3$ powder with the yield of over 80% could be obtained. Then the obtained powder was pressed into 4 inch Cu dish at mechanical force of 4 tons for 30 min and then the $LaNiO_3$ sputtering target, shown in Fig. 2.2(b), was fabricated. .

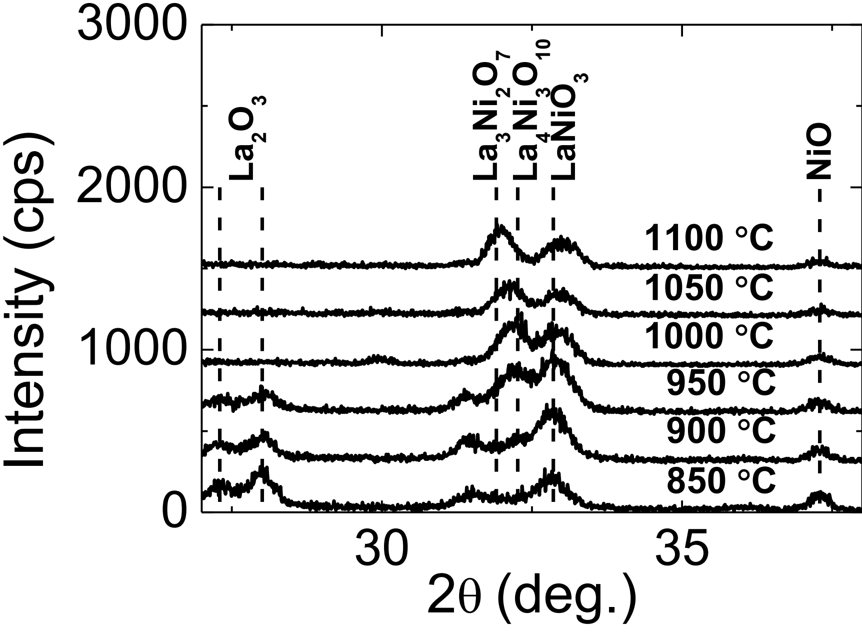

Fig. 2.1: XRD profiles of $LaNiO_3$ powders prepared at from 850-1100 ºC.

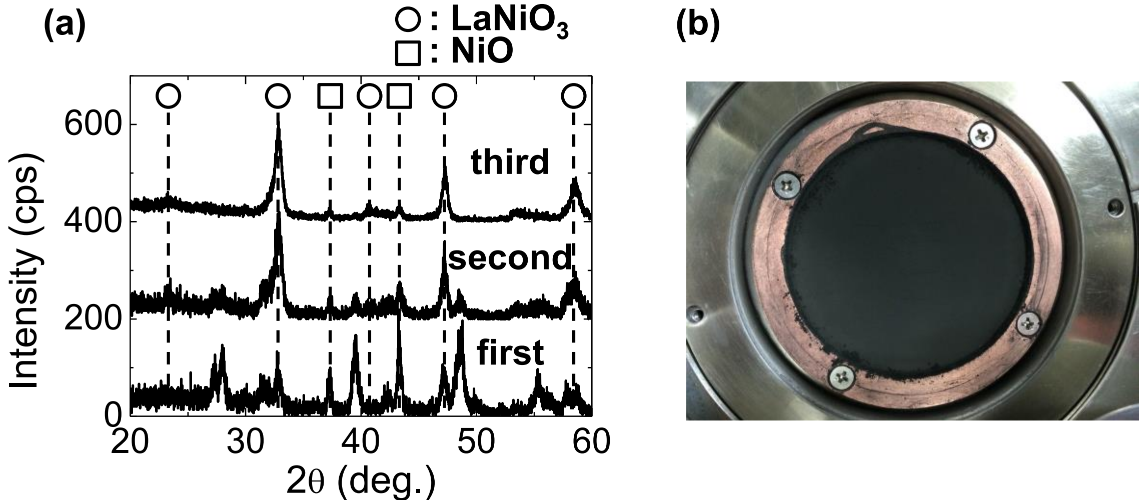

Fig. 2.2 Prepared $LaNiO_3$ (a) powders, prepared at 850ºC, and (b) the powder target.

2-2-2 Preparation of $LaNiO_3$ and $BiFeO_3$ Thin Films

The schematic illustration of rf-sputter utilized for the deposition of $LaNiO_3$ film is depicted in Fig. 2.3. SiO_2/(100)Si wafers were used as substrates and cleaned in acetone and ethanol for 5 min sequentially in an ultrasonic bath. Sputtering was carried out at an rf power of 50 W and a working pressure of 10^{-2} Torr. A mixture of O_2 (30 %) and Ar (70 %) was introduced into the deposition chamber during the growth.

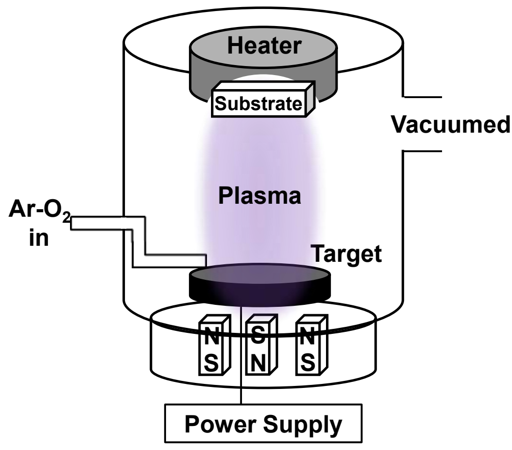

Fig. 2.3: Schematic illustration of the rf-sputter.

BiFeO$_3$ films were prepared by the sol-gel method using a 0.2 mol BiFeO$_3$ precursor solution (Kojundo Chemical Laboratory) on the prepared LaNiO$_3$ films. After spin-coating at 3000 rpm for 30 s, the films were dried to remove organic solvent at 150 ºC for 1 min. Then, the films were prebaked to decompose organic matter in the film at 300 ºC for 3 min. This cycle was repeated 3 times. After that, the BiFeO$_3$ thin films were crystalized at 500 ºC for 10 min. Moreover, these steps were repeated 3 times to obtain 250±10nm-thick films. To measure the macroscopic electrical properties, the circular Pt top electrodes (ϕ=0.1 - 0.4 mm) were deposited by using rf magnetron sputtering at room temperature.

2-2-3 Structural and Electrical Characterization of LaNiO$_3$ and BiFeO$_3$ Films

The crystal structure of the prepared films was characterized by high-resolution X-ray diffraction (XRD) analysis and XRD reciprocal space mapping (RSM) (Panalytical X-pert Pro). The resistivity of the LaNiO$_3$ thin films was measured by the four-point probe method at RT. The microstructures and composition of the films were characterized by field-emission scanning electron microscopy (FE-SEM; Hitachi S-4500) with energy dispersive X-ray spectroscopy (EDX). The dielectric and ferroelectric properties were measured using an LCR meter (Agilent 4284A) and a Sawyer-Tower circuit, respectively.

2-2-4 Observation of Domain Structure and Characterization of Converse Piezoelectric Properties using Piezoelectric Force Microscopy

The surface morphologies and ferroelectric domain structure of the films were observed by atomic force microscopy (AFM) and piezoelectric force microscopy (PFM) techniques using a scanning probe microscopy (SPM; SII NanoNAvi). The schematic of set-up for AFM/PFM is shown in Fig. 2.4. The mapping measurements of the out-of-plane (OP) and in-plane (IP) piezoelectric responses were carried out by applying an AC voltage of 1 V and 4 kHz. The electric field-strain curves were also measured on single domain of the $BiFeO_3$ films by applying a unipolar or bipolar AC voltage of 5 Hz. The voltage was applied to the bottom electrode in the PFM measurement, while the voltage was applied to the top electrode in other measurements. To avoid confusion, the electric field toward the bottom electrode is defined as positive in this chapter. All the PFM and strain curve measurements were carried out at the area without a top electrode. The effective longitudinal piezoelectric coefficient $d_{33,\mathrm{AFM}}$ was determined from the incline of the strain curves.

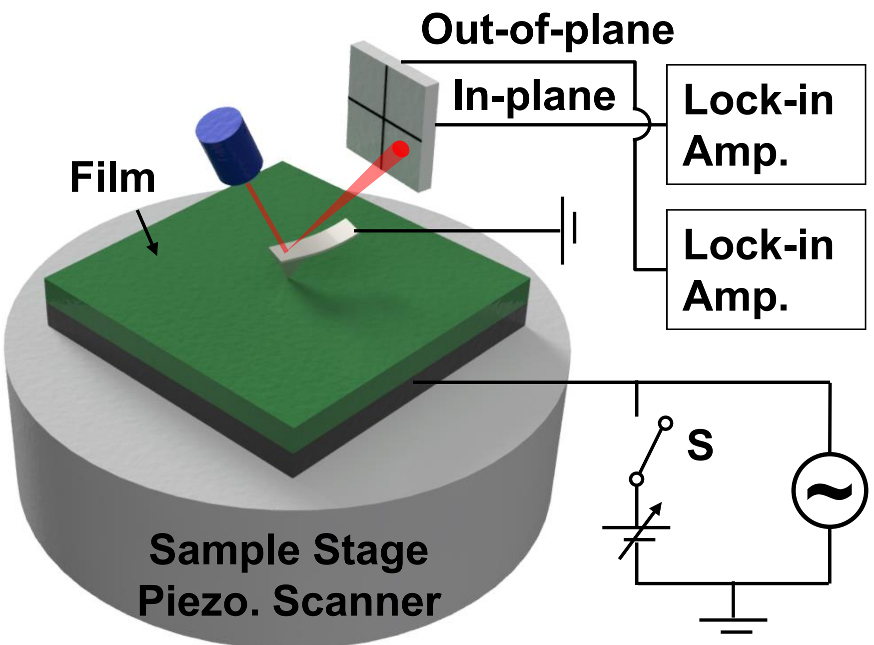

Fig. 2.4: Set-up for AFM/PFM measurement. When unipolar strain curve of a film is measured. switch: S is turned on and the DC bias is added to the applied AC voltage.

2-2-4 Characterization of Direct Piezoelectric Properties using Wafer Bending Technique

The direct piezoelectric responses of the $BiFeO_3$ thin films were measured by applying strain to the samples and collecting developed charges.[12] The set-up image is shown in Fig. 2.5. The sample was attached on an Al plate (1×15×0.2 cm^3). The strain was applied periodiclly to the sample by bending the Al plate using an actuator. The induced charge via the direct piezoelectric response was measured using a lock-in amplifier (NF LI5640). The strain was measured using a strain gage (KFG-02-120-C1-11L1M2R). The $e_{31,f}$ coefficient was calculated using eq. (2.1)

$$e_{31,f} = \frac{I_0}{2\pi f S(1-\upsilon)x_1} \tag{2.2}$$

where the I_0, S, υ, and x_1 and f are current induced by direct piezoelectric effect,

area of top electrode, poison's ratio, and strain and the frequency. All the films were measured by applying the strain of 50μ. The details of the measurement are described elsewhere [13].

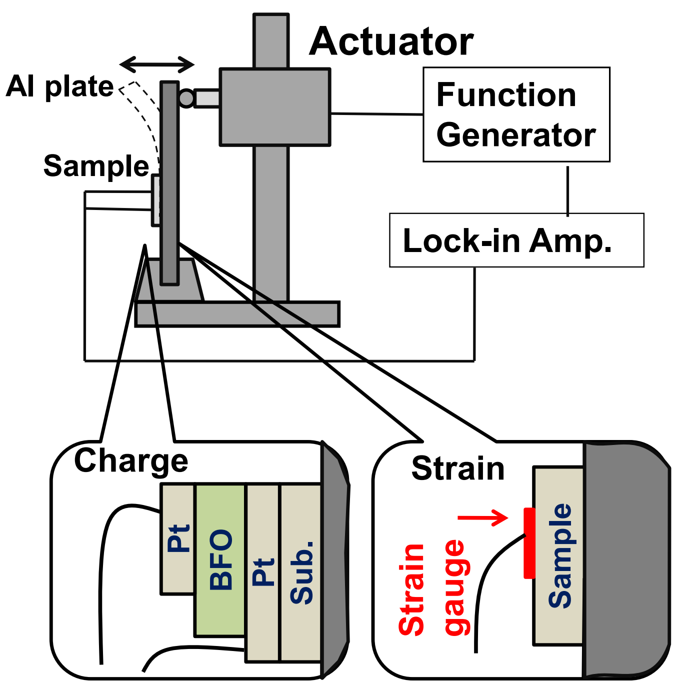

Fig. 2.5: Set-up for measuring direct piezoelectric properties.

2-3 Results and discussion

2-3-1 Fundamental Properties of Prepared $LaNiO_3$ Films

Figure 2.6(a), (b) show the 2θ-ω XRD patterns of the $LaNiO_3$ bottom electrode deposited at 150-500 ºC for 3h. As can be seen, all the films have preferential (100) orientation. The diffraction peaks of the films also shift to lower angle with increase in the crystallization temperature. The c-axis lattice constant of $LaNiO_3$ films is shown in Fig 2.6(c). The as-deposited films have lattice constant from 3.92-3.96 Å which is much

larger than the reported lattice constant (3.84Å). From the result of the analysis of the composition ratio of La/Ni shown in Fig. 2.6(d), it is found that all the prepared films have approximately La/Ni≅1. These results indicate that the as-deposited films have a large amount of defects such as oxygen deficiencies. The resistivity of prepared $LaNiO_3$ films was also the order of 10^{-4} Ω·cm except for that of the film deposited at 150 ºC shown in Fig. 2.7. Therefore, the films, deposited at ≥ 300 ºC, were used as electrode and template for $BiFeO_3$ films

In order to recover the vacancies, the films were annealed in O_2 atmosphere at 500-800 ºC. The effects of the annealing on the lattice constant of the (100)-oriented $LaNiO_3$ thin films were investigated by XRD. Figure 2.8(a) shows the 2θ-ω profiles around the 200 diffraction of the $LaNiO_3$ thin films. The shifts of the diffraction peak to a lower angle with increasing the annealing temperature indicate the decrease of the lattice constant along the out-of-plane direction ($d_{(100)\perp}$). The lattice constants along the in-plane direction ($d_{(100)//}$) were also determined by XRD RSM. Figure 2.8(b) shows the XRD RSM pattern of the as-deposited $LaNiO_3$ thin film. Similar patterns were obtained on the annealed films. $d_{(100)//}$ of $LaNiO_3$ thin films was determined from the interplanar spacing of (110) and $d_{(100)\perp}$ of the films. The dependence of $d_{(100)\perp}$ and $d_{(100)//}$ for the $LaNiO_3$ films on the annealing temperature is shown in Fig. 2.8(c). $d_{(100)\perp}$ of the as-deposited film is close to that of bulk $BiFeO_3$ (3.96 Å). It decreases and approaches that of bulk $LaNiO_3$ (3.84 Å) with increasing annealing temperature. In contrast, $d_{(100)//}$ of all the films are almost the same. The volume of the unit cell of $LaNiO_3$ was decreased by annealing. The resistivity was 2.6×10^{-3} Ω·cm for the as-deposited film and decreases to 7.7×10^{-4} Ω·cm with increasing the annealing temperature. The change of

the volume of the unit cell and resistivity of $LaNiO_3$ by the annealing can be explained by the decrease of the oxygen deficiencies.

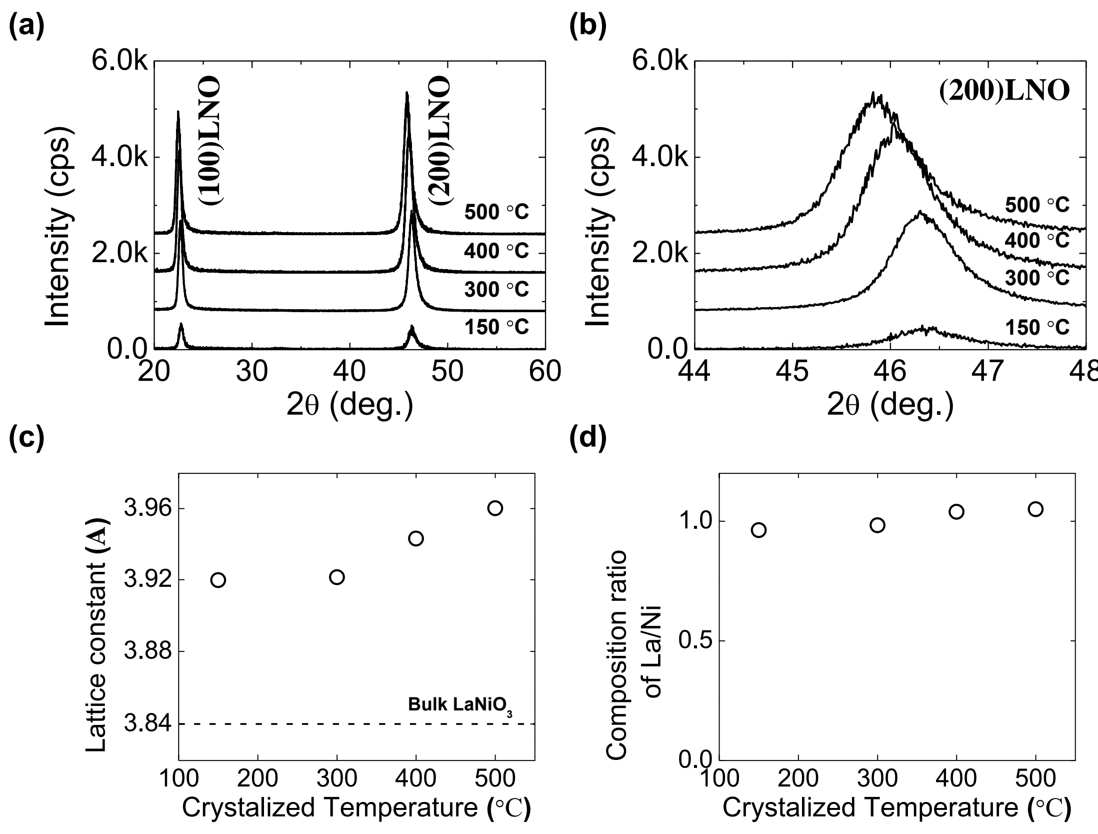

Fig. 2.6: (a), (b) XRD patterns of $LaNiO_3/SiO_2/Si$ substrates. Crystalized temperature dependence of (c) the c-lattice constant and (d) composition ratio of La/Ni.

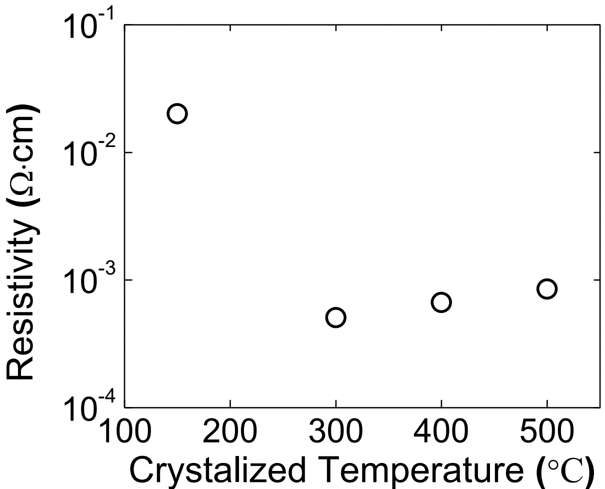

Fig. 2.7: Resistivity dependence on the crystalized temperature of $LaNiO_3$ films.

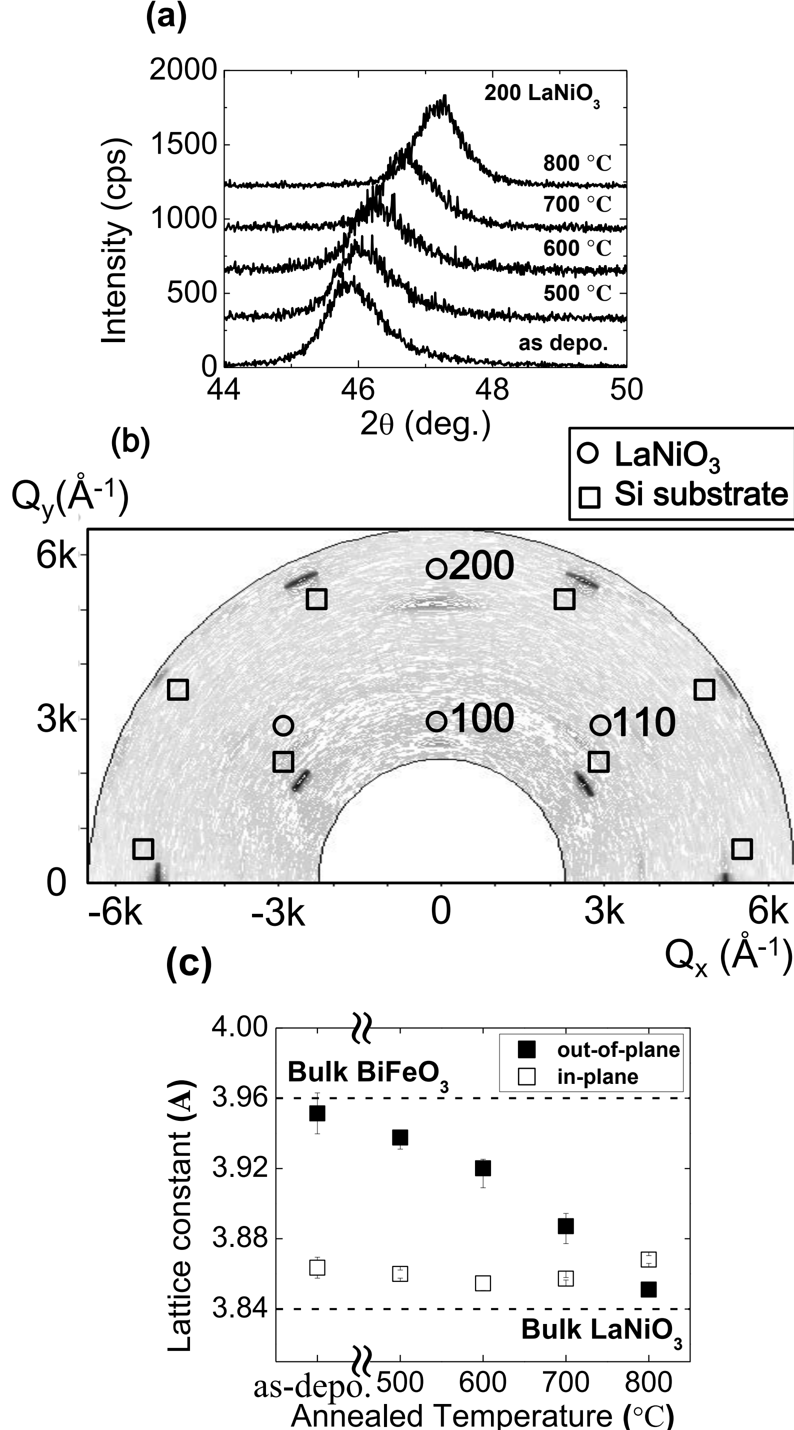

Fig. 2.8: XRD patterns of (a) as-deposited and annealed (200)$LaNiO_3$ on SiO_2/Si substrate, (b) XRD RSM pattern of the as-deposited LaNiO3 thin film, and (c) annealing temperature dependence of the lattice constant along the out-of-plane and in-plane directions

2-3-2 Piezoelectric Properties of (100) Orientated $BiFeO_3$ Thin Films

The $BiFeO_3$ thin films were crystalized between 450 and 600 °C on the (100)$LaNiO_3$ deposited on /SiO_2/ (100)Si at 300 ºC and annealed at 700ºC. The XRD profiles of the films, which is shown in Fig. 2.9(a), indicated that the $BiFeO_3$ films show (100) preferential orientation without any secondary phases or misoriented grains. On a (111)Pt/Ti/SiO_2/Si substrate, a polycrystalline $BiFeO_3$ film is grown under the same preparation condition. Figure 2.9(b) shows the XRD profiles around the (200) diffraction peak of the $BiFeO_3$ films. The (200) diffraction peaks of all the films shift to a higher angle compared with the bulk, which indicates that all the films have a smaller lattice constant (3.92–3.93 Å) than the bulk (3.96 Å). The lattice constant increases with increasing annealing temperature. It appears that a smaller lattice constant is attributed by thermal strain because the thermal expansion coefficient of Si (0.3×10^{-5} K^{-1}) is smaller than that of $BiFeO_3$ (0.6×10^{-5} K^{-1}).

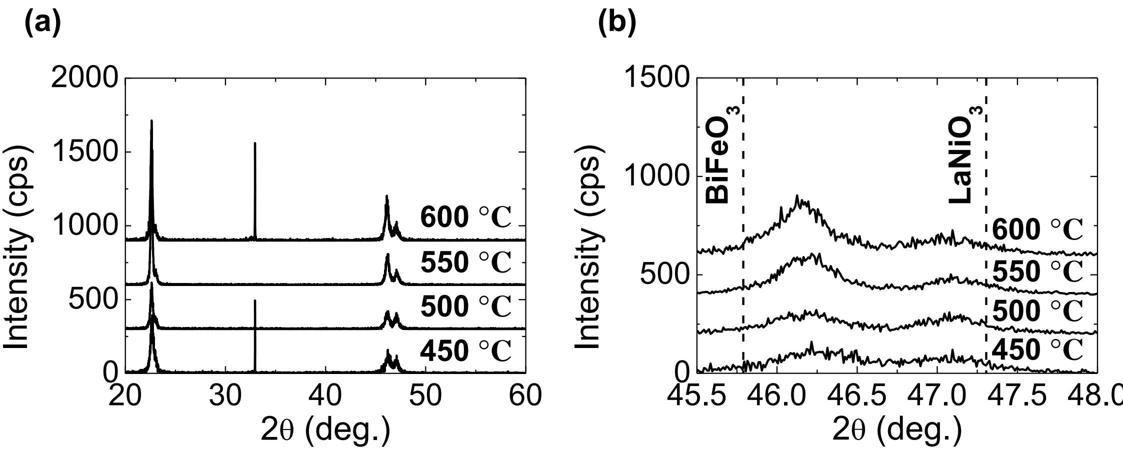

Fig. 2.9: XRD patterns of (a) $LaNiO_3$/SiO_2/Si substrate and (b) $BiFeO_3$ films, crystallized by annealing at 450, 500, 550, and 600 °C, on the $LaNiO_3$/SiO_2/Si substrates.

The cross sections of the (100) oriented $BiFeO_3$ films on (100)$LaNiO_3/SiO_2/Si$ were observed by FE-SEM. The micrographs are shown in Fig. 2.10. The $BiFeO_3$ films annealed at 450 and 500 °C show a layered granular structure, which corresponds to the annealing temperature. In contrast, the films deposited at 550 and 600 °C show a columnar structure. The dielectric properties of the (100) oriented $BiFeO_3$ films are shown in Fig. 2.11. The dielectric constant of the films annealed below 500 °C is about 100 and that of the films crystalized at 550 and 600 °C increases to 140. The increase in the dielectric constant corresponds to the change of the microstructure of the $BiFeO_3$ film, as shown in Fig. 3. The dielectric losses of all the films are 0.8–2.0% in the frequency range from 1 kHz to 1 MHz. The film crystalized at 600 °C shows an increase in the dielectric loss with decreasing frequency, which indicates that the film has a larger leakage current than the other films.

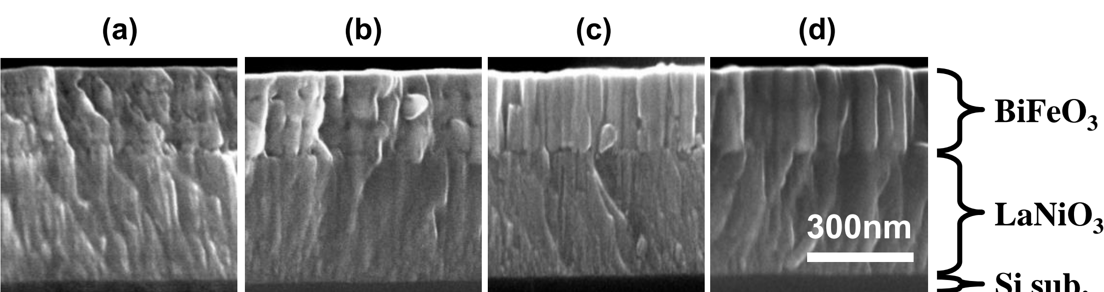

Fig. 2.10: Cross section of the $BiFeO_3$ films crystallized at (a) 450, (b) 500, (c) 550, and (d) 600 °C.

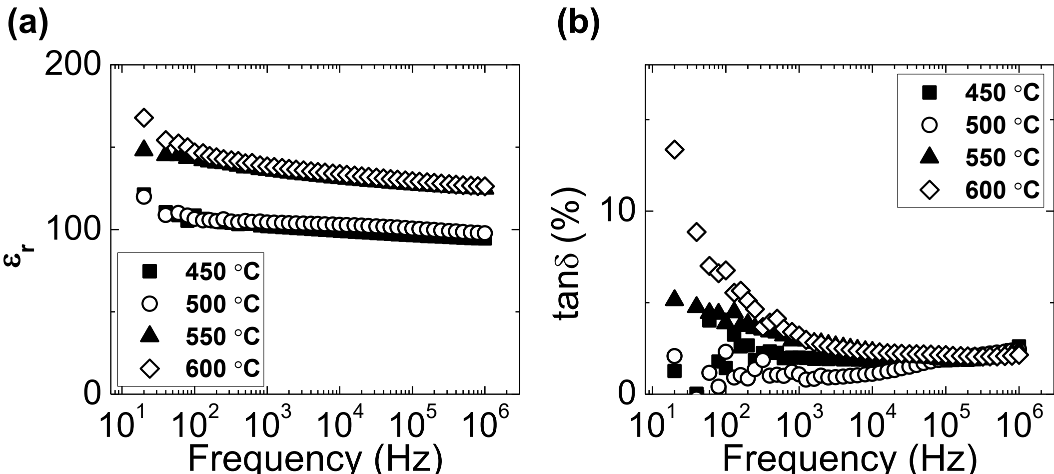

Fig. 2.11: Frequency dependence of (a) dielectric constant (ε_r) and (b) dielectric loss (tanδ) of the (100) oriented $BiFeO_3$ crystallized by annealing at 450, 500, 550, and 600 °C.

The P–E hysteresis loops of the films shown in Fig. 2.12 indicate that all the films have ferroelectricity. An AC voltage with a frequency of 100 kHz was used for the measurement. The remanent polarization of the film crystallized at 600 °C is significantly larger than the others. It appears that the shift of the P–E hysteresis loops to the negative bias is originated from the asymmetric structure of the sample, because the shift is not observed for the samples with the $Pt/BiFeO_3/Pt$ structure shown in Fig. 2.13.

The surface morphologies, and OP and IP piezoelectric responses were observed using SPM, as shown in Fig. 2.14. The surface morphologies shown in the top images indicate that the grain size increases with increasing the annealing temperature. The mapping images of the OP piezoelectric response shown in the middle images indicate that the downward domain is dominant in all the films, which is consistent with

the shifts of P–E hysteresis loops. From the mapping images of the IP piezoelectric response shown in bottom, it was found that the domain size also increases with increasing annealing temperature. To investigate the relationship between the annealing temperature and the piezoelectric properties, the electric field-strain curves were measured by SPM. The results of the (100) oriented $BiFeO_3$ film crystallized at each temperature are shown in Fig. 2.15(a). From the incline of the electric field-strain curves in the negative electric field region, the $d_{33,\mathrm{AFM}}$ coefficient was calculated, as shown in Fig. 2.15(a). The relationship between the annealing temperature and the $d_{33,\mathrm{AFM}}$ coefficient is shown in Fig. 2.15(b). The $d_{33,\mathrm{AFM}}$ coefficient of the film crystalized at 450 °C is 42±8 pm/V. With increasing annealing temperature, the $d_{33,\mathrm{AFM}}$ coefficient increases to 56±5 pm/V, which is slightly smaller than that of the epitaxial $BiFeO_3$ films. Since the $d_{33,\mathrm{AFM}}$ coefficient was determined from the piezoelectric resonance in a microscopic region, the $d_{33,\mathrm{AFM}}$ coefficient is dominated by the intrinsic contribution. Therefore, it appears that the increase in the $d_{33,\mathrm{AFM}}$ coefficient with increasing annealing temperature is mainly caused by the increase in the remnant polarization.

The $e_{31,\mathrm{f}}$ coefficients of the films, which is the most important parameter of the piezoelectric films for Piezoelectric VEHs, were characterized. The measurement was carried out without poling treatment, because the $BiFeO_3$ films were self-polarized, as shown in Figs. 2.12 and 2.14. The $e_{31,\mathrm{f}}$ coefficients and k_{31}^2 derived from $e_{31,\mathrm{f}}$ and ε_r as a function of the annealing temperature are shown in Fig. 2.16(a),(b). The $e_{31,\mathrm{f}}$ coefficient increases with increasing annealing temperature. This behavior is similar to that of the intrinsic $d_{33,\mathrm{AFM}}$ coefficient. However, the increase in the $e_{31,\mathrm{f}}$ coefficient of the (100) orientated films from the annealing temperature of 450 to 600 °C is more than twofold,

which is larger than that of the $d_{33,AFM}$ coefficient (~50%). Since the $e_{31,f}$ coefficient was determined by the piezoelectric response from a macroscopic region, this result indicates that the $e_{31,f}$ coefficient is influenced by the microstructure of the film as well as the intrinsic contribution, which relates to the $d_{33,AFM}$ coefficient. As shown in Fig. 6, the larger domain size is obtained at a higher crystalized temperature. Therefore, it is suggested that the increase in the domain size increases the $e_{31,f}$ coefficient, which is different from the previous reports. It appears that the difference is caused by the microstructure of the films. As shown in Fig. 6, the domain size is similar to or larger than the grain size, which indicates that the most of the grains are single domain. Therefore, it seems that the domain walls observed by the IP piezoelectric response exist at the grain boundary. Under this condition, a small domain size has an adverse effect on the $e_{31,f}$ coefficient. The maximum $e_{31,f}$ coefficient (-4.1 C/m^2) is obtained at the annealing temperature of 600 °C, which is 8.7 times larger than that of the polycrystalline films ($e_{31,f}$ = -0.47 C/m^2) and comparable to that of the (100) epitaxial films. The maximum k_{31}^2 of the films is 6.3%, which is more than 54 times larger than that of the polycrystalline films.

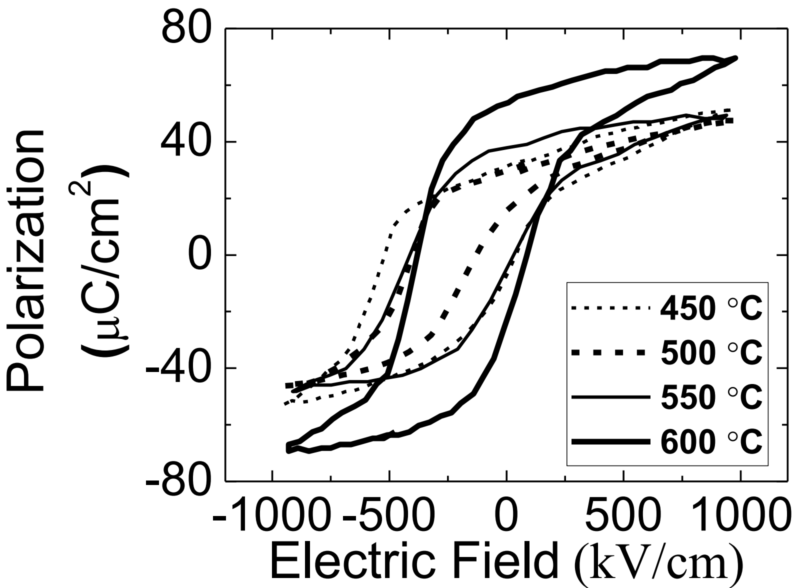

Fig. 2.12: Ferroelectric hysteresis loops of the (100) oriented $BiFeO_3$ films crystallized by annealing at 450, 500, 550, and 600 °C

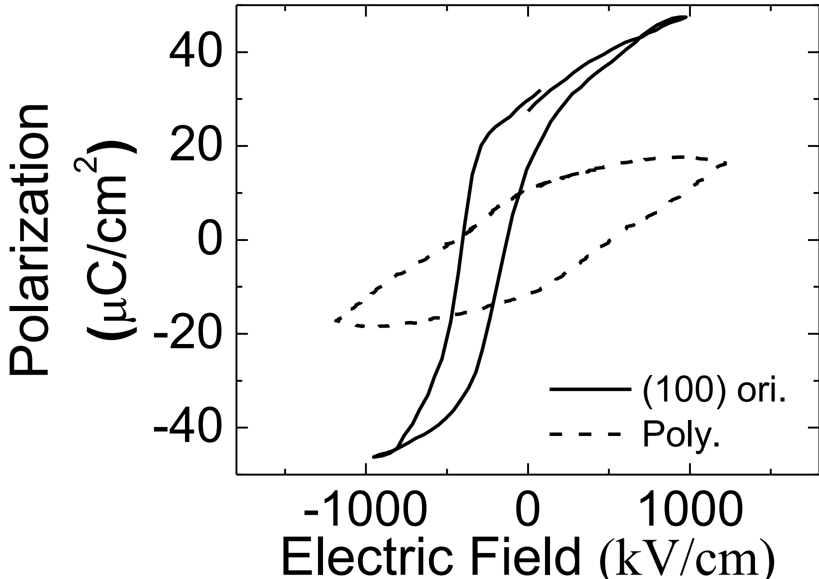

Fig. 2.13: Ferroelectric hysteresis loops of the (100) orientated (solid line) and polycrystalline (dotted line) $BiFeO_3$ films

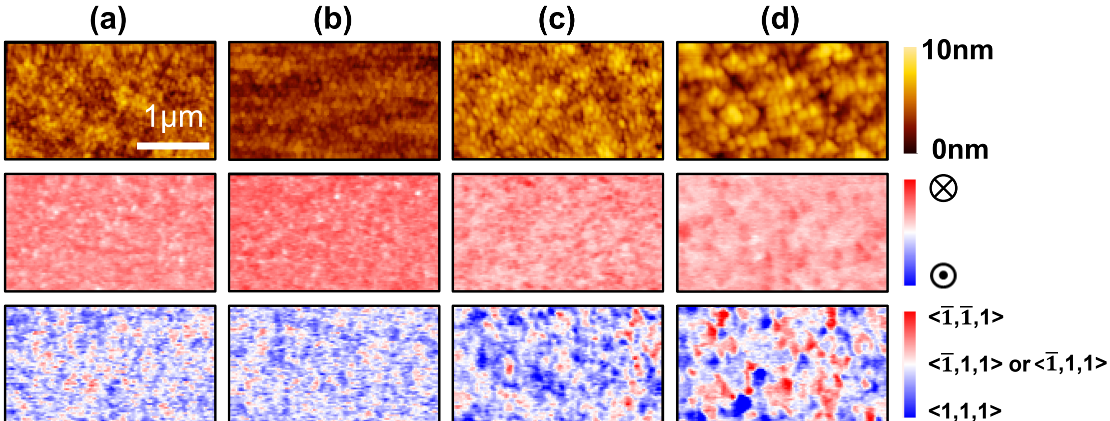

Fig. 2.14: Surface morphologies (top) and OP and IP domain structures (middle and bottom) of the (100) oriented $BiFeO_3$ films crystallized by annealing at (a) 450, (b) 500, (c) 550, and (d) 600 ºC.

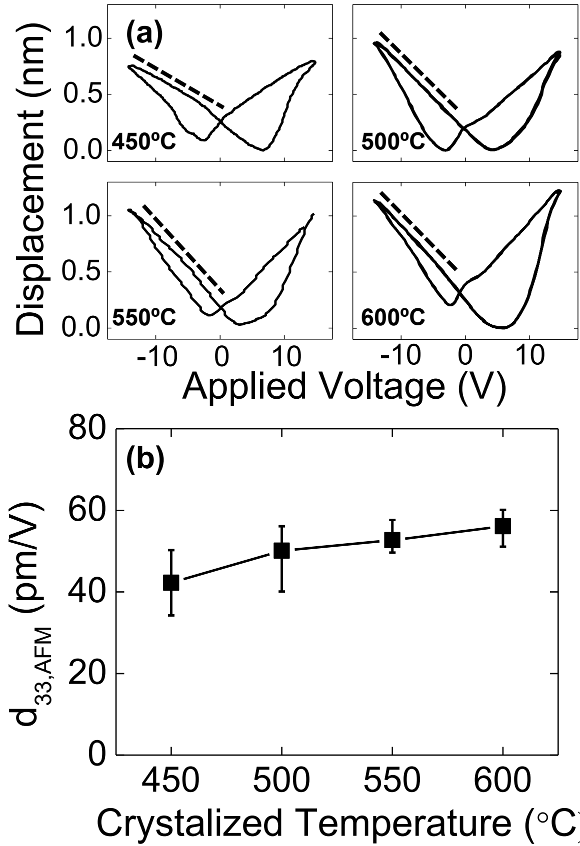

Fig. 2.15: Inverse piezoelectric responses: (a) strain-voltage curves of the (100) oriented $BiFeO_3$ films crystallized by annealing at 450, 500, 550, and 600 °C, and (b) $d_{33,AFM}$ coefficient as a function of the annealing temperature.

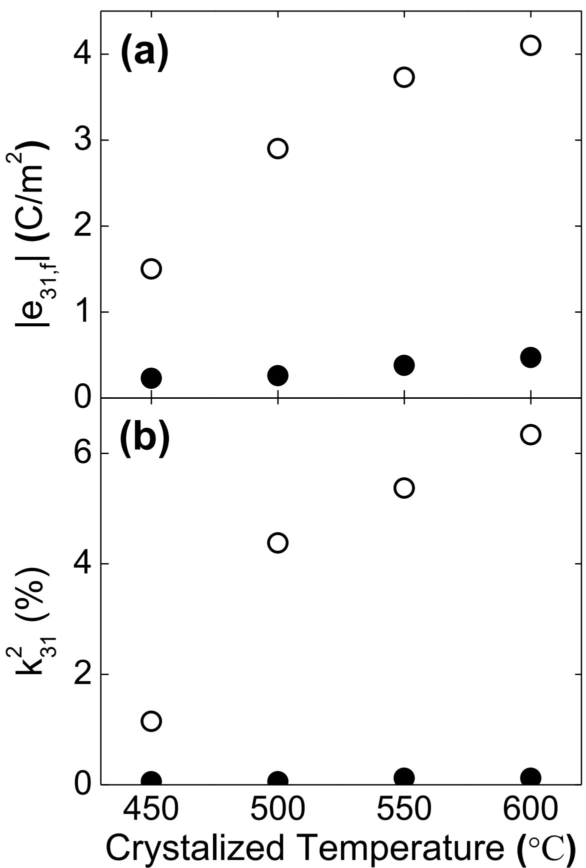

Fig. 2.16: Crystalized temperature dependences of (a) the $e_{31,f}$ coefficient and (b) k_{31}^2 coefficient of (100 orientated (white) and polycrystalline (black) $BiFeO_3$ films.

2-3-2 Enhancement of Piezoresponse of (100) Orientated $BiFeO_3$ Films by In-plane Tensile Stress

The $BiFeO_3$ films were also deposited on the as-deposited and annealed (100) $LaNiO_3$ films. The list of the samples is shown in Table 2.1. The XRD 2θ-ω profiles shown in Fig. 2.17 indicate that the (100)-oriented $BiFeO_3$ films without secondary phases or misoriented grains are obtained on the $LaNiO_3$ electrodes. The $d_{(100)\perp}$ and $d_{(100)//}$ of the $BiFeO_3$ films were determined in the same way as those of the $LaNiO_3$

electrodes. The results are shown in Fig. 2.18(a). No significant dependence of the $d_{(100)\perp}$ and $d_{(100)//}$ on the annealing temperature of the $LaNiO_3$ electrodes is observed. Figure 2.18(b) shows the lattice distortion ($d_{(100)\perp}/d_{(100)//}$) of the $BiFeO_3$ films calculated from the $d_{(100)\perp}$ and $d_{(100)//}$ shown in Fig. 2.18(a). As can be seen, the crystal structures of the $BiFeO_3$ films were distorted by the in-plane tensile stress. In addition, $d_{(100)//}$ of $BiFeO_3$ is larger than that of $LaNiO_3$, which indicates that the in-plane distortion is not caused by the lattice misfit. Therefore, the distortion is caused by the thermal strain induced by the difference inthe thermal expansion coefficients of (100)Si (0.3×10^{-5} K^{-1}) and $BiFeO_3$ (0.6×10^{-5} K^{-1}).

Table 2.1: Summary of the properties of the (100)-orientated $BiFeO_3$ films.

	sample A	sample B	sample C	sample D
$LaNiO_3$ annealed at (°C)	×	600	700	800
distortion	0.989	0.988	0.988	0.990
ε_r	140	133	136	132
P_r (μC/cm^2)	27	26	27	27
$d_{33,AFM}$ (pm/V)	46	58	63	64
$e_{31,f}$ (C/m^2)	-2.4	-4.0	-3.1	-2.4
k_{31}^2 (%)	3.0	8.5	3.7	2.3

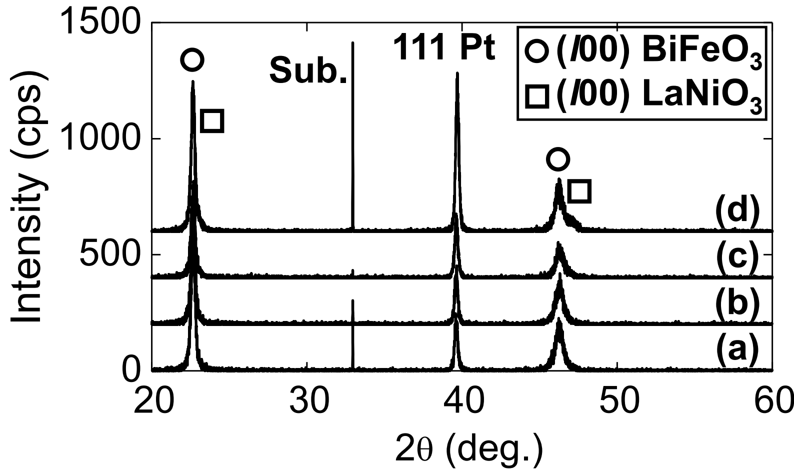

Fig. 2.17: XRD patterns of $BiFeO_3$ thin film deposited on (a) as-deposited $LaNiO_3$ film and on the $LaNiO_3$ films annealed at (b) 600, (c) 700, and (d) 800 °C, which correspond to samples A, B, C, and D, respectively.

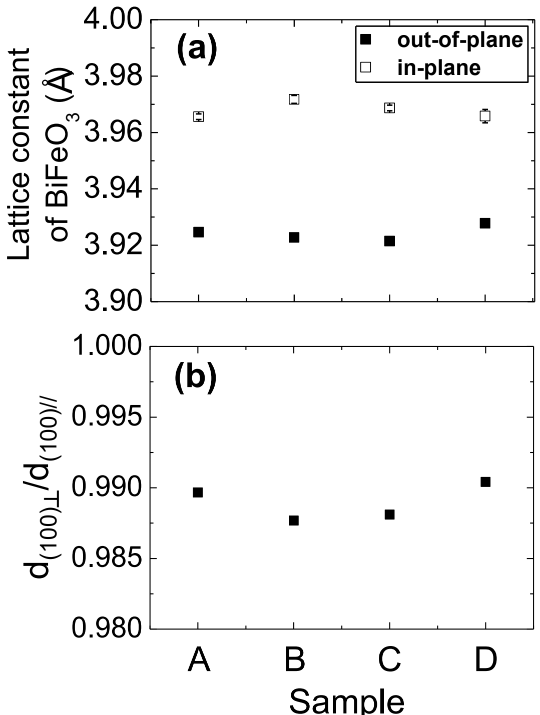

Fig. 2.18: (a) $d_{(100)\perp}$ and $d_{(100)//}$ and (b) $d_{(100)\perp}/d_{(100)//}$ of samples A, B, C, and D.

The electrical properties of the (100)-oriented $BiFeO_3$ thin films were characterized. The frequency dependences of the dielectric constants and dielectric losses were measured. The dielectric constants for all the films were about 130-140 at 20 Hz, which was independent of the annealing temperature of the $LaNiO_3$ films, and were constant against the frequency. The dielectric losses of all the films were about 1.0% at 100 kHz. The polarization-electric field (P-E) hysteresis loops of the films measured at 100 kHz and room temperature are shown in Fig. 2.19. While no significant dependence of the P-E loops on the $d_{(100)\perp}/d_{(100)//}$ of the $BiFeO_3$ films is recognized, all the P-E loops were shifted to negative bias. The saturated polarizations Psat and positive remnant polarization $+P_r$ are 45 - 49 and 27 μC/cm^2, respectively, which are almost independent ofthe annealing temperature.

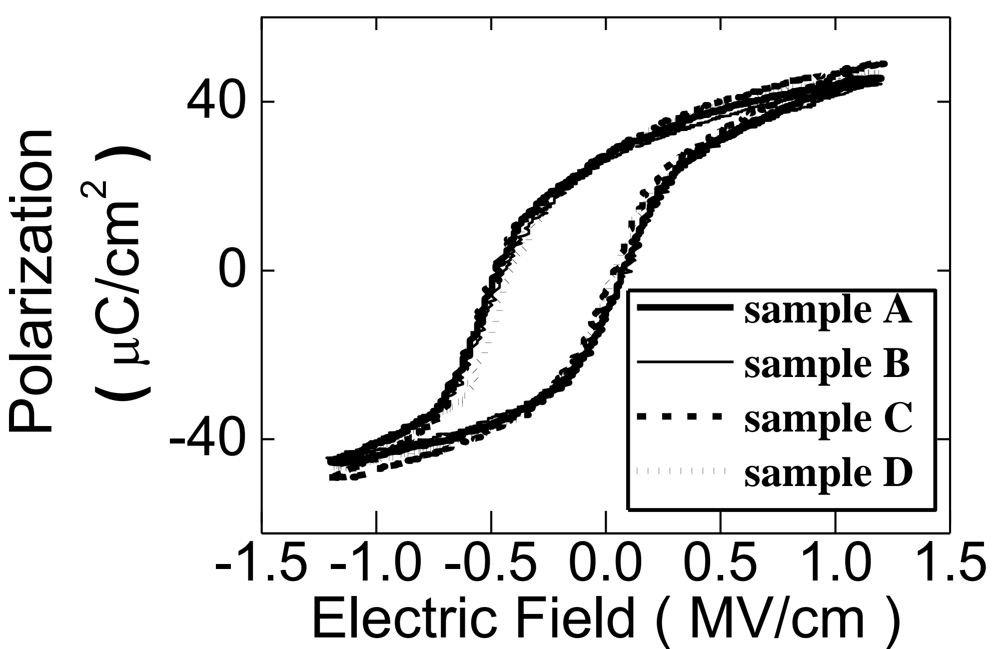

Fig. 2.19: P-E hysteresis loops of samples A, B, C, and D.

The surface morphologies, OP, and IP piezoelectric response of the $BiFeO_3$ films are shown in Fig. 2.20. The Acosθ signals, where A is the amplitude of the piezoelectric response and θ is the phase of the piezoelectric response, are used for the PFM images. All the films show the grain size of about 40-80 nm. OP PFM images indicate that the spontaneous polarization of the $BiFeO_3$ films is self-polarized downward, which corresponds to the shift of the P-E hysteresis loops. The IP PFM images indicate that the domain sizes of samples A, B, C, and D were almost same. Figure 2.21 shows the strain curves measured at 5Hz using SPM. The positive electric field was applied to avoid the influence of the domain wall motion. However, slight hysteresis behavior was observed for all the films. The $d_{33,\mathrm{AFM}}$ coefficients of samples A, B, C, and D were 46, 58, 63, and 64 pm/V, respectively. The $d_{33,\mathrm{AFM}}$ coefficient increases with increasing annealing temperature. Although $d_{33,\mathrm{AFM}}$ ideally corresponds to the intrinsic piezoelectric response because of the microscopic measurement in a particular domain, it is suggested that the $d_{33,\mathrm{AFM}}$ coefficient is influenced by the extrinsic contribution.

The $e_{31,\mathrm{f}}$ coefficient of $BiFeO_3$ films, which is quite important for the Piezoelectric VEH application, was characterized without poling treatment because the $BiFeO_3$ films were self-polarized as described above. The $e_{31,\mathrm{f}}$ coefficients of samples A, B, C, and D were -2.4, -4.0, -3.1, and -2.4 C/m^2, respectively. Although the $e_{31,\mathrm{f}}$ coefficient does not depend on the annealing temperature, it was found that the $e_{31,\mathrm{f}}$ coefficient increases with decreasing $d_{(100)\perp}/d_{(100)//}$, as shown in Fig. 2.22(a). The k_{31}^2 also shows similar behavior [Fig. 2.22(b)]. A summary of the results of the samples is shown in Table 2.1. Liu et al. predicted theoretically that $BiFeO_3$ thin films distorted to

the in-plane tensile direction have an orthorhombic-rhombohedral phase boundary [19]. Although further investigation is needed, it is possible that the increase of the $e_{31,f}$ coefficient is caused by the in-plane tensile strain as well as the in-plane compressive strain [20]. The maximum $e_{31,f}$ and k_{31}^2 are -4.0 C/m^2 and 8.5%, respectively, which are comparable to those of epitaxial $BiFeO_3$.

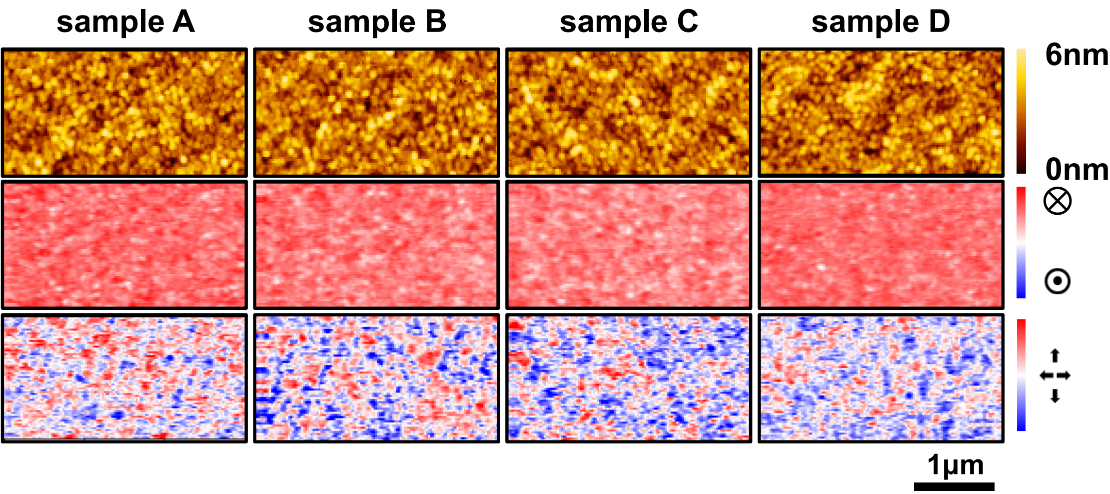

Fig. 2.20: Surface morphologies (top) and OP and IP domain structures (middle and bottom) of samples A, B, C, and D.

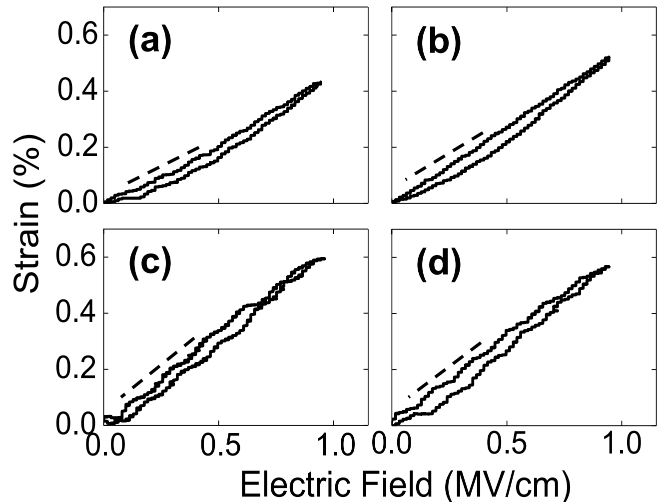

Fig. 2.21: Strain-electric field curves of samples A, B, C, and D.

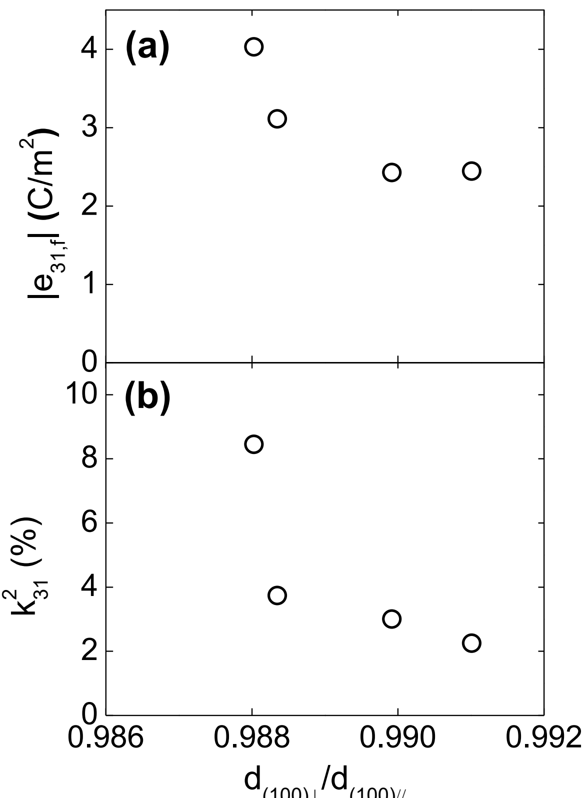

Fig. 2.22: Dependences of (a) $e_{31,f}$ coefficient and (b) k^2_{31} on $d_{(100)\perp}/d_{(100)//}$ of the $BiFeO_3$ films.

2-4 Conclusions

(100) oriented $BiFeO_3$ thin films were deposited by using $LaNiO_3$ bottom electrodes, which have preferential (100) orientation, on Si substrates by sol-gel method. From the cross section of the films, it was found that the growth configuration changes from layered granular structure characterized by the sol-gel method to a columnar structure with an increase in annealing temperature. All the prepared films have downward spontaneous polarization in the virgin state and the grain and domain sizes become larger with increasing annealing temperature. From the measurement of the piezoelectric properties of these films, the $e_{31,f}$ increase as the domain size is larger than the grain size. It is concluded that the decrease of domain wall, which is clamped by the grain boundary, causes the enhancement. The obtained maximum direct piezoelectric properties, the $e_{31,f}$ and k_{31}^2 of the (100) oriented $BiFeO_3$ film, which has a columnar structure and the largest grain and domain sizes among the films, were also -4.1 C/m^2 and 6.3%, respectively.

Furthermore, It was found that the $e_{31,f}$ and k_{31}^2 of the (100)-oriented $BiFeO_3$ film increased with decreasing $d_{(100)\perp}$ /$d_{(100)//}$ of the $BiFeO_3$ thin films. The largest $e_{31,f}$ and k_{31}^2 were -4.0 C/m^2 and 8.5%, respectively, which are comparable to those of epitaxial (100)$BiFeO_3$ thin films (10 %).

These results indicate that the (100) orientation control of $BiFeO_3$ on Si can enhance the piezoelectric properties significantly and the domain and crystal structure of the film influence the piezoelectric properties.

References

[1] K. Ujimoto, T. Yoshimura, A. Ashida, and N. Fujimura Appl. Phys. Lett. **100,** 102901 (2012).

[2] T. Yoshimura, K. Ujimoto, Y. Kawahara, K. Wakazono, K. Kariya1, N. Fujimura, and S. Murakami, Jpn. J. Appl. Phys. **52,** 09KA03 (2013).

[3] K. Ujimoto, Ph. D. Dissertation in Osaka Prefecture University.

[4] X. J. Meng, J. G. Cheng, J. L. Sun, H. J. Ye, S. L. Guo, and J. H. Chu, J. Cryst. Growth **220**, 100 (2000).

[5] L. Yang, G. Wang, C. Mao, Y. Zhang, R. Liang, C. Soyer, D. Remiens, and X. Dong, J. Cryst. Growth **311**, 4241 (2009).

[6] C.-C. Yang, M.-S. Chen, T.-J. Hong, C.-M. Wu, J.-M. Wu, and T.-B. Wu, Appl. Phys. Lett. **66**, 2643 (1995).

[7] M.-J. Shyu, T.-J. Hong, T.-J. Yang, and T.-B. Wu, Jpn. J. Appl. Phys. **34**, 3647 (1995).

[8] H. Ichinose, M. Nagano, H. Katsuki, and H. Takagi, J. Mater. Sci. **29**, 5115 (1994).

[9] Y.-H. Lee, C.-S. Liang, and J.-M. Wu, Electrochem. Solid-State Lett. **8**, F55 (2005).

[10] F. Yan, T. J. Zhu, M. O. Lai, and L. Lu, J. Appl. Phys. **110**, 084102 (2011).

[11] S. H. Baek, J. Park, D. M. Kim, V. A. Aksyuk, R. R. Das, S. D. Bu, D. A. Felker, J. Lettieri, V. Vaithyanathan, S. S. N. Bharadwaja, N. Bassiri-Gharb, Y. B. Chen, H. P. Sun, C. M. Folkman, H. W. Jang, D. J. Kreft, S. K. Streiffer, R. Ramesh, X. Q. Pan, S. Trolier-McKinstry, D. G. Schlom, M. S. Rzchowski, R. H. Blick, and C. B. Eom: Science **334**, (2011) 958.

[12] M.-A. Dubois and P. Muralt, Sens. Actuators **77**, 106 (1999).

[13] T. Yoshimura, H. Sakiyama, T. Oshio, A. Ashida, and N. Fujimura, Jpn. J. Appl. Phys. **49**, 021501 (2010).

[14] C. J. C. Bennett, H. S. Kim, M. Varela, M. D. Biegalski, D. H. Kim, D. P. Norton, H. M. Meyer, and H. M. Christen, J. Mater. Res. **26**, 1326 (2011).

[15] T. Yoshimura, K. Ujimoto, Y. Kawahara, K. Wakazono, K. Kariya, N. Fujimura, and S. Murakami, Jpn. J. Appl. Phys. **52**, 09KA03 (2013).

[16] S. Wada, K. Yako, H. Kakemoto, T. Tsurumi, and T. Kiguchi, J. Appl. Phys. **98**, 014109 (2005).

[17] F. Kubel and H. Schmid, Acta Crystallogr., Sect. B **46**, 698 (1990).

[18] R. D. Sánchez, M. T. Causa, A. Caneiro, A. Butera, M. Vallet-Regí, M. J. Sayagués, J. González-Calbet, F. García-Sanz, and J. Rivas, Phys. Rev. B **54**, 16574 (1996).

[19] Y. Y. Liu, L. Yang, and J. Y. Li, J. Appl. Phys. **113**, 183524 (2013).

[20] T. Yoshimura, K. Ujimoto, Y. Kawahara, K. Wakazono, K. Kariya, N. Fujimura, and S. Murakami, Jpn. J. Appl. Phys. **52**, 09KA03 (2013).

Chapter 3: Fabrication and Characterization of Electromechanical Transduction Properties of Piezoelectric MEMS Vibrational Energy Harvester Using $BiFeO_3$ Lead-Free Ferroelectric Films

3-1 Introduction

In previous Chapter, it was found that (100)-orientated $BiFeO_3$ films, grown on Si substrate, exhibited large electromechanical coupling coefficient (k_{31}^2). The maximum transverse piezoelectric stress confident and electromechanical coupling coefficient of the (100)-orientated film was -4.0 C/m^2 and 8.5%, comparable with the epitaxial $BiFeO_3$ films [1-5]. The fabrication of high performance piezoelectric VEHs can be expected by using the $BiFeO_3$ films.

In this chapter, the piezoelectric VEHs with the $BiFeO_3$ films are fabricated and the electromechanical transduction properties of the VEHs under various vibration conditions are characterized. From the physical value obtained from the experimental results, the required performances of piezoelectric films in the application of VEHs are discussed.

3-2 Experiment Procedure

3-2-1 Fabrication of Piezoelectric MEMS VEHs with $BiFeO_3$ Films

The structure of the fabricated piezoelectric MEMS VEHs of the present study is shown schematically in figure 3.1. It consists of a single cantilever structure, which is composed of a supporting silicon membrane, $LaNiO_3$/Pt/Ti bottom electrode, BFO

piezoelectric film, Pt upper electrode, and Cu proof mass. A schematic of the MEMS fabrication process of VEHs is shown in figure 3.2. The starting material was a silicon-on-insulator (SOI) wafer with 5-µm-thick Si, 1-µm-thick SiO_2 (insulating layer), and 650-µm-thick Si-bulk. The structures of the VEHs were fabricated as follows; 1) An SOI wafer was oxidized on both sides with a thickness of 0.5 µm. 2) Thin diaphragm structures were formed using the anisotropic etching technique with TMAH (25 wt%, 90 ºC) etchant. An important point here is to stop etching, saving a final diaphragm with about 100-µm-thick Si-bulk, so as to take care of process-handling in the post-process flow. 3) We used $LaNiO_3$/Pt/Ti films as bottom electrodes. The thicknesses of $LaNiO_3$, Pt, and Ti were 150, 200, and 20 nm, respectively. The Pt/Ti film was deposited on the front surface by sputtering, and patterned using a lift-off technique to form the bottom electrode. The $LaNiO_3$ film was deposited by sputtering, and patterned by wet-etching with HCl etchant for 15s. 4) A piezoelectric BFO thin film was prepared by the sol-gel method. The film was crystallized by annealing at 500 ºC for 10 min in a rapid thermal annealing furnace. The BFO film was patterned by etching with a etchant of HF(50%):HCl:H_2O=1:1:20 for 45s. 5) The Pt upper electrode with a thickness of 200 nm was formed by sputtering and a lift-off technique. 6) To form the cantilevers, the SiO_2 and Si layers on the front surface around the cantilevers were removed completely by BHF etchant and by reactive ion etching (RIE) with SF_6 reactive gas, respectively. 7) The Si-bulk and insulator layer below the cantilever were all etched out by RIE with SF_6 reactive gas and by BHF etchant, respectively. 8) A proof mass made of Cu was attached at the free end of the cantilever. The proof mass was attached onto the tip of Piezoelectric VEHs to control the resonant frequency to around 100 Hz.

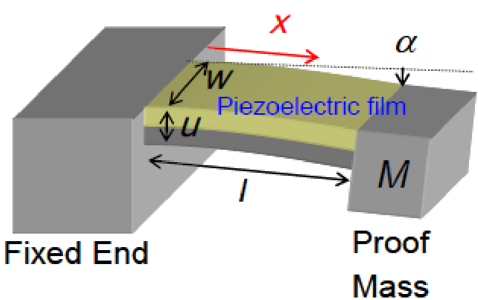

Fig. 3.1: Structure of piezoelectric VEHs.

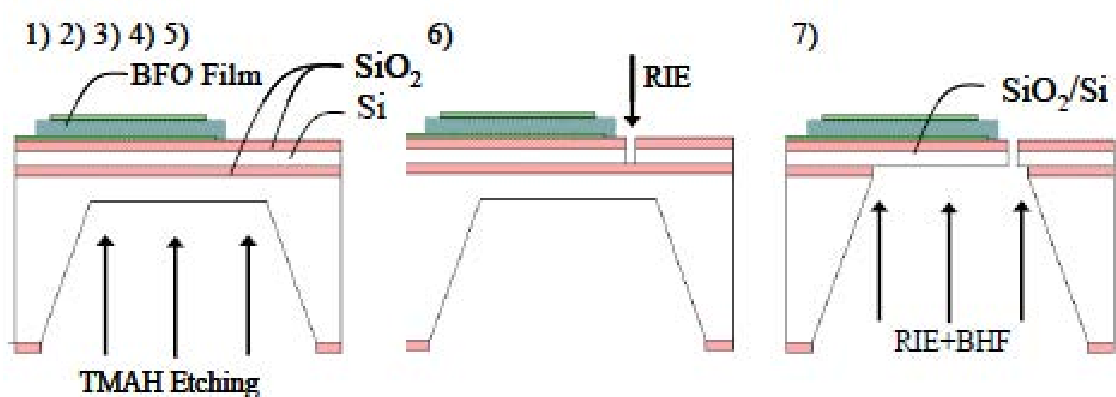

Fig. 3.2: Fabrication of a Piezoelectric VEH using the MEMS technique.

.

We could finally fabricate the piezoelectric VEHs with unimorph structure, as shown in figure 3.3. In this chapter, 3 types of Piezoelectric VEHs with 350nm-thick polycrystalline, 250nm-thick (100) orientated, and 450nm-thick (100) orientated $BiFeO_3$ films were prepared. The length, width, and thickness of the cantilevers were 3 mm, 0.4 mm, and 6 μm, respectively. Therefore, the effective volume of the fabricated Piezoelectric VEHs was 0.40×3.0×0.256 mm^3.

3-2-3 Measurement Set-Up for Characterizing the Electromechanical Transduction Properties

The experimental setup with a vibrator for measuring the electromechanical properties of the fabricated MEMS Piezoelectric VEHs is shown in figure 3.4. Vibrations were applied to the VEHs toward the vertical direction using a shaker. We applied several waves to the shaker to characterize the output power of the VEHs under ideal and random vibrations. Figure 3.5 depicts profiles of these vibrational waves, which have the following specifications: wave 1 (fundamental wave of 92.3 Hz), wave 2 (fundamental wave + sub-harmonic wave of 46.15 Hz), wave 3 (fundamental wave + harmonic wave of 184.6 Hz), and wave 4 (fundamental wave + harmonic wave + sub-harmonic wave). Each were prepared by a function generator (HP 33120A, Hewlett Packard). The amplitude of each vibration was the same. The applied acceleration was measured using an accelerometer (352A24, PCB Piezotronics, inc.). The displacement of the cantilever was determined using a laser head LK-020 and laser displacement sensor (LK-G5000, Keyence Corporation). To characterize the generated electrical power of the VEH, a load resistance was connected to the $BiFeO_3$ film. The output voltage across the load resistor was measured using a lock-in amplifier (LI5640, NF Corporation). These systems are controlled by LabVIEW.

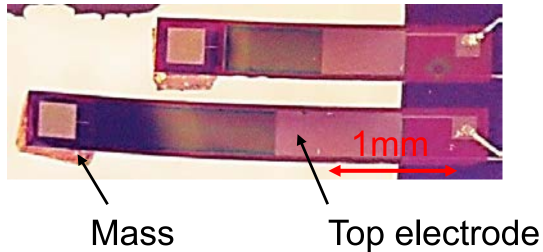

Fig. 3.3: Photo of a piezoelectric VEHs device with a $BiFeO_3$ films..

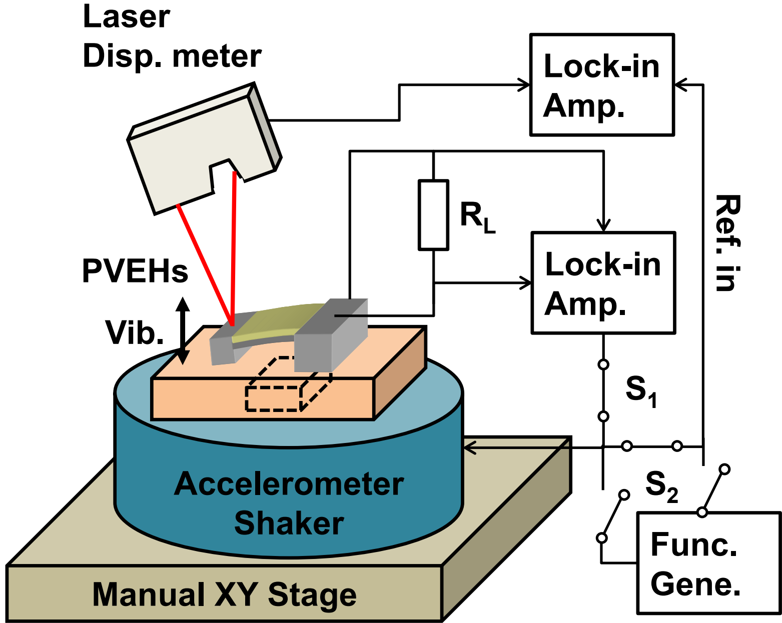

Fig. 3.4: Experimental setup with a shaker for measuring the electromechanical properties of piezoelectric VEHs. S_1 and S_2 are turned on when the ideal and random oscillation is applied to the piezoelectric VEHs, respectively.

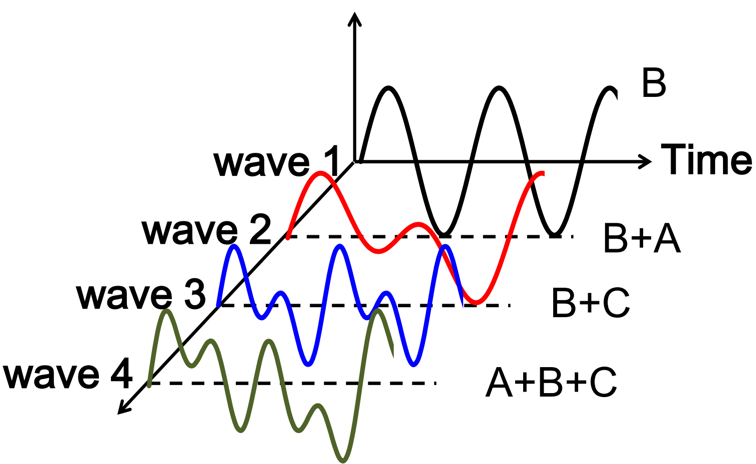

Fig. 3.5: Prepared random oscillation.

3-3 Results and Discussion

3-3-1 Output Power Under Ideal Vibration

The vibration frequency dependence of the normalized output voltage of the piezoelectric VEHs using $BiFeO_3$ film is shown in figure 3.6. The accelerations of the applied vibrations were 0.009, 0.018 and 0.054 G_{rms}. It can be seen that the Piezoelectric VEHs have a resonance frequency around 91-95 Hz and that the normalized maximum output voltage at the resonance frequency is independent of the acceleration. In contrast, hysteresis behaviors were observed near the resonance frequency and the non-linear resonance increased with increasing acceleration. It appears that the nonlinear resonance of the piezoelectric VEHs mainly originates from the dumping effect of air and the nonlinear elasticity of the cantilever [6] The maximum voltage of piezoelectric VEHs with 350nm-thick polycrystalline, 250nm-thick (100) orientated, and 450nm-thick (100) orientated films are 1.5, 2.7, and 8.7 $V \cdot G^{-1}$.

The load resistance dependence of the output power density of the piezoelectric VEHs with the $BiFeO_3$ films were characterized at each accelerations and the resonance

frequency as shown in figure 3.7. The output power is the electrical power that is dissipated in the load resistance, and normalized using G^2 and the effective area of the VEH. The maximum normalized output power of the piezoelectric VEHs using 350nm-thick polycrystalline, 250nm-thick (100) orientated, and 450nm-thick (100) orientated films are 0.70, 2.6, 10 $\mu W \cdot mm^{-2} \cdot G^{-2}$ at load resistances of impedance marching, respectively. This result is comparable to or larger than those of the best-performing VEHs using other piezoelectric films including $Pb(Zr,Ti)O_3$ films [7].

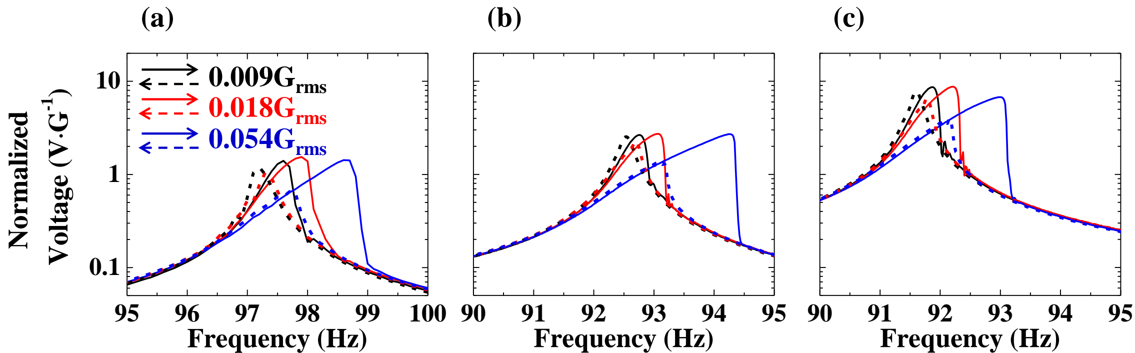

Fig. 3.6: Normalized output voltage as a function of vibration frequency of piezoelectric VEHs with (a) 350nm polycrystalline, (b) 250nm (100) orientated, and (c) 450nm (100) orientated $BiFeO_3$ films.

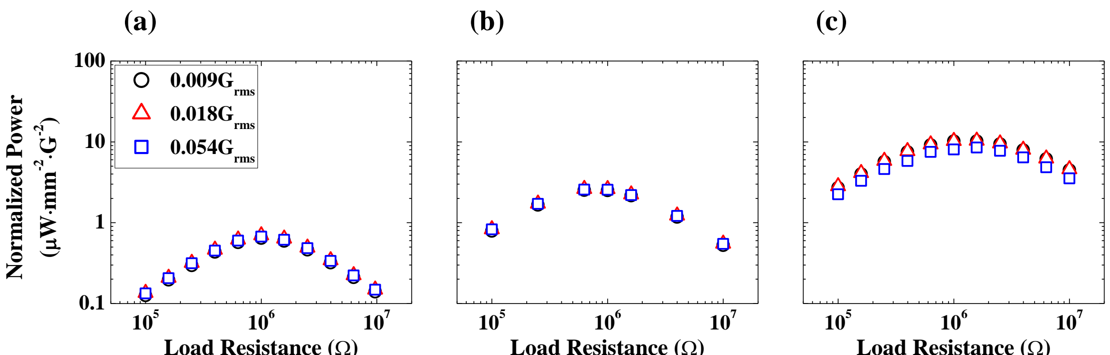

Fig. 3.7: Load resistance dependence of the normalized output power of piezoelectric VEHs with (a) 350nm polycrystalline, (b) 250nm (100) orientated, and (c) 450nm (100) orientated $BiFeO_3$ films.

3-3-2 Characterization of the Electromechanical Transduction Properties

To estimate the performance of fabricated VEHs quantitatively, Electromechanical coupling coefficient of piezoelectric VEHs is regularly characterized by,

$$K^2 = \frac{\omega_{oc}^2}{\omega_{oc}^2 - \omega_{sc}^2} \tag{3.1}$$

where, K^2 is electromechanical coupling coefficient of the structure and ω_{oc} and ω_{sc} are open and short circuit [8]. However, frequency change of the fabricated VEHs at open and short circuit could not be observed. On the other hand, the load resistance dependence on output power and quality factor, calculated from frequency properties, shows clearly changes at the vicinity of a 1MΩ of impedance matching as shown in Fig.3.8. These indicate the energy transfer effectively around the point of impedance matching. Another model was employed to estimate K^2.

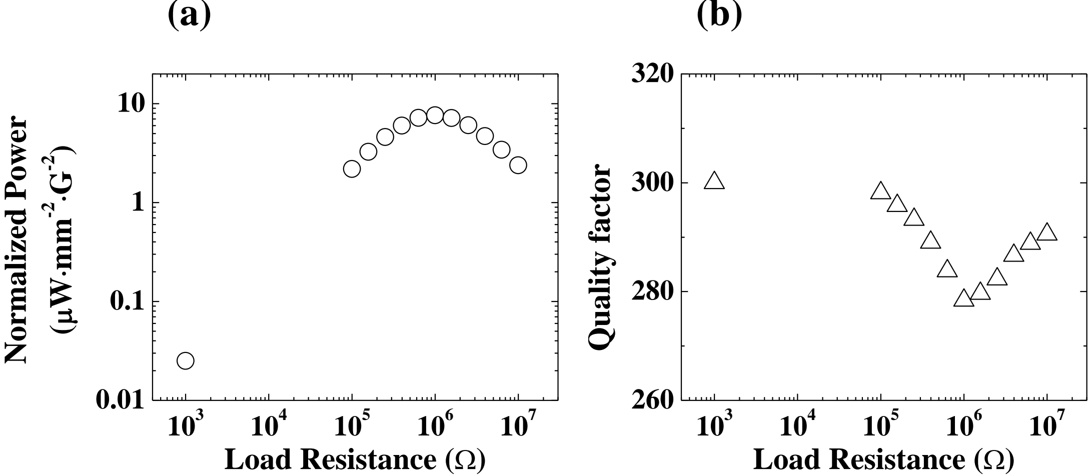

Fig. 3.8: Load resistance dependence on (a) normalized power and (b) quality factor of piezoelectric VEHs with 450nm (100) orientated $BiFeO_3$ film.

The lumped model of the VEHs, including mechanical and electrical domains, is given by Fig. 3.9 [9]. From this equivalent circuit, the governing equation, based on Duffing equation and Kirchhoff equation, could be written as,

$$m\ddot{x} + c(\dot{x} - \dot{y}) + k_1(x - y) + k_3(x - y)^3 = -\theta V \tag{3.2}$$

$$\theta(\dot{x} - \dot{y}) = -i_c - i_R = C_p\dot{V} + \frac{V}{R_l} \tag{3.3}$$

where *m, c,* k_1, k_3, C_p and R_l are proof mass, damping coefficient, spring constant, non-linear spring constant, capacitance of piezoelectric materials and applied load resistance. *V* is also generated voltage and *x* and *y* are the displacement of tip of cantilever and the base. Form eq. (1) and (2), energy balance could be given by,

$$k_1 XY\pi sin(-\phi) - \pi\omega c_m(X^2 - 2XYcos\phi + Y^2) = \frac{\pi V^2}{\omega R_l} \tag{3.4}$$

θ is also given by using electromechanical coupling coefficient of the structure (K^2)

$$K^2 = \frac{\theta^2}{k_1 C_p} \tag{3.5}$$

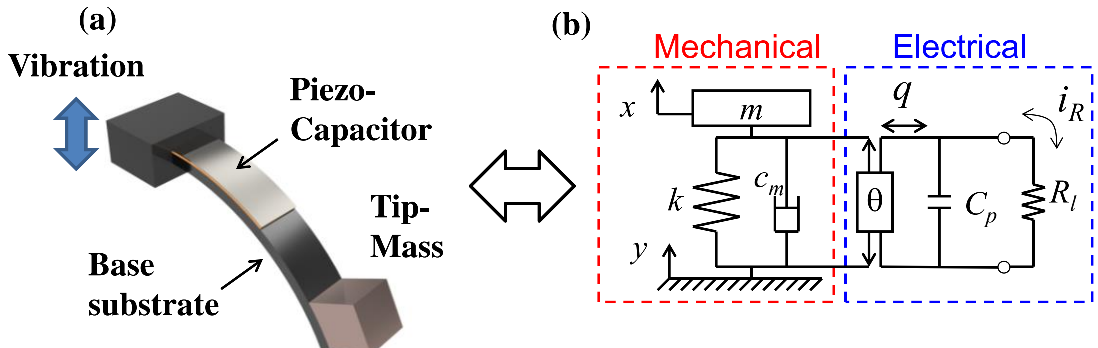

Fig. 3.9: Schematic figure of the MEMS VEHs and the equivalent circuit.

From the equation (3.4), experimental input energy (Ei), dissipated energy (Ed), electrical generated energy (Ee), and Ei-Ed were calculated as shown in Fig. 3.10. Since

the Ee and Ei-Ed is almost consistent, It indicates that the measurement results of electromechanical properties of the VEHs is reasonable. The generated Efficiency, where Ee is divided by Ei, and K^2 are calculated in Fig. 3.11. The efficiency has maximum point and it indicates that the energy is transferred most effectively. In contrast, K^2shows almost constant value (0.32%). Equation 3.5 indicates that the k_{31}^2 is 4.3 %, is corresponding with that obtained from equation 2.1. To characterize the performance of the VEHs, theoretical electromechanical properties of VEHs is calculated as shown in Fig. 3.12. the calculation is performed using experimentally obtained values, are assumed as m=0.64 mg, k_1=0.21 N/m, k_3=0 N/m, Q=300, C_p=1.7 nF, and A=0.009G_{rms}.

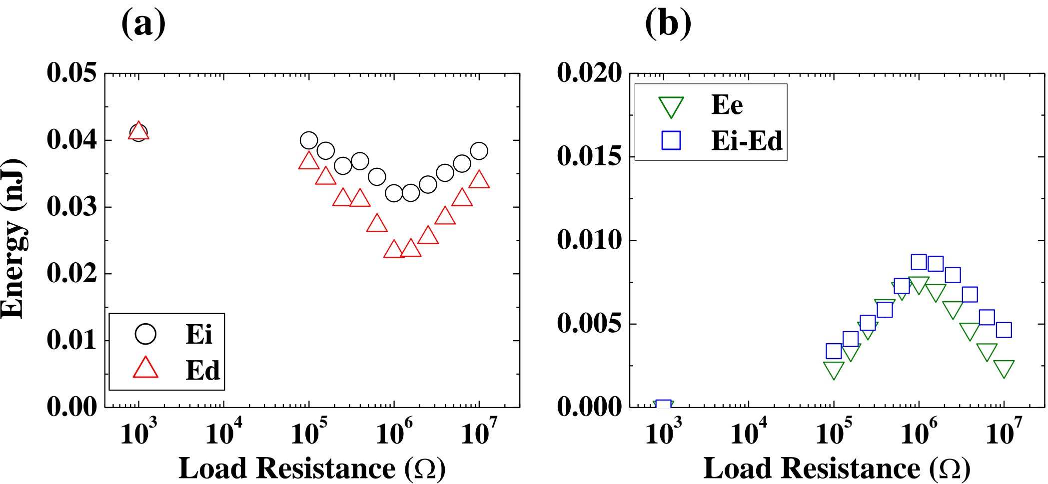

Fig. 3.10: Energy as a function of load resistance of piezoelectric VEHs with 450nm (100) orientated $BiFeO_3$ film.

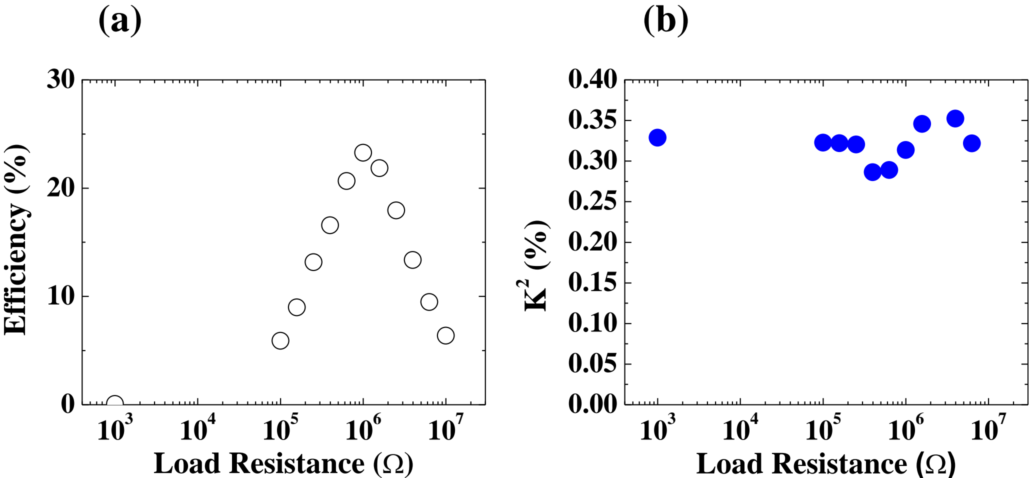

Fig. 3.11: Load resistance dependence on (a) efficiency and K^2 of piezoelectric VEHs with 450nm (100) orientated $BiFeO_3$ film.

The calculation results show that the tip displacement decreases as it approaches to the impedance matching or K^2 increases. This indicates that the mechanical energy is absorbed by piezoelectric thin films. On the other hand, the output power increases by a specific point with increasing K^2 at impedance matching and then the value decreases at over the point. Similar response could be observed at different load resistance. These behaviors expand like V-shape on Fig. 3.12. Too large K^2 prevents the electrical power generation and shifts the impedance matching. These results indicate that VEHs has optimal electromechanical coupling coefficient and the value of MEMS scale piezoelectric VEHs is approximately K^2 ≈1.0 %. Since the fabricated $BiFeO_3$ films and the VEHs have k_{31}^2 =4.4 % and K^2 =0.32 % as shown in Fig. 2.16 and Fig. 3.11, the piezoelectric thin films with k_{31}^2 of approximately 10 % have to be selected to obtain theoretical maximum output in energy harvesting application .

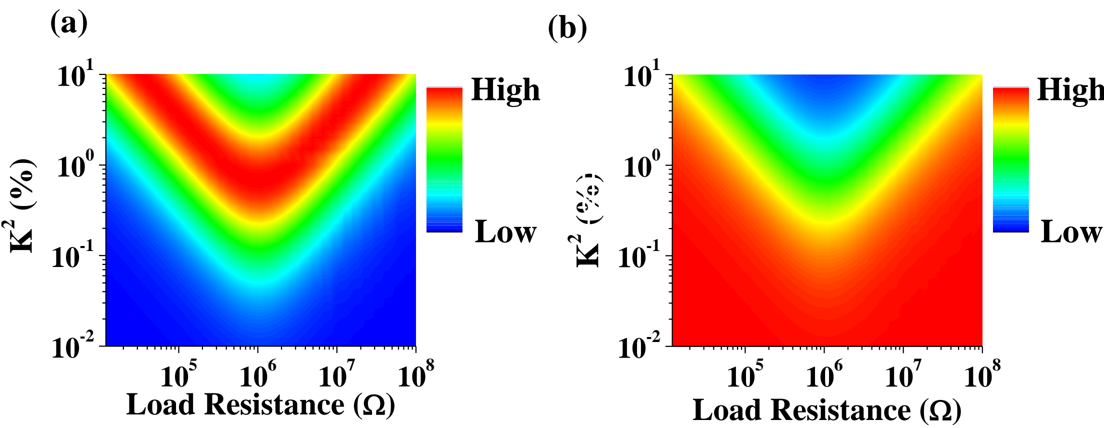

Fig. 3.12: Numerical calculated (a) output power and (b) displacement properties.

3-3-3 Electromechanical Transduction Properties under Random Oscillations

The results described above sections were obtained using monochromatic vibrational waves. However, environmental vibrations have random oscillations comprising various frequencies and amplitudes. Here, to discuss the influence of the spurious components on VEH performance, the displacement and output power of the VEHs with 250nm-thick (100) orientated $BiFeO_3$ film were characterized using vibrations composed of the fundamental, harmonic, and sub-harmonic waves. Figure 3.13 shows the waveforms of the input vibrational acceleration and displacement of the tip of the cantilever under waves 1–4 as shown in Fig. 3.5. Each displacement waveform is different from that for acceleration under random vibrations and all the waveforms look roughly sinusoidal. This indicates that only a single frequency component is included in each wave. The results of fast Fourier transform analysis

indicate that the VEH responds only to the resonance vibration of 92.3 Hz, which is the resonant frequency of the VEHs. Nevertheless, the displacement amplitude under random vibrations is smaller than that under an ideal vibration of the fundamental; the maximum accelerations of waves 1–4 are similar.

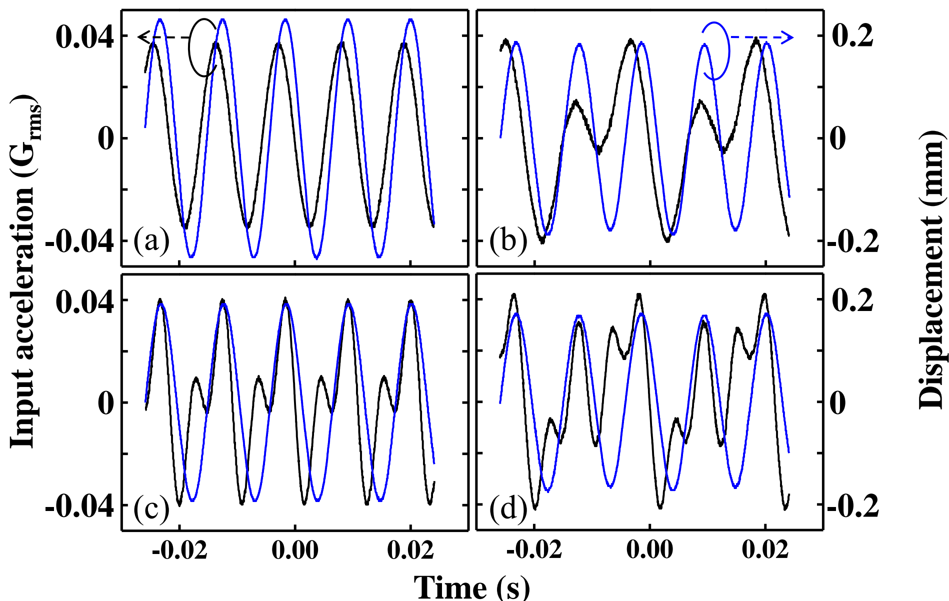

Fig. 3.13: Waveform of input acceleration and displacement under (a) wave 1, (b) wave 2, (c) wave 3, and (d) wave 4.

The waveforms of acceleration were also Fourier analysed. Figure 3.14 shows that the ratios of the maximum acceleration of waves 2–4 with respect to wave 1. The displacement calculated using the acceleration ratio and the maximum displacement at wave 1 (0.232 mm) are 0.148, 0.167, and 0.128 mm for waves 2, 3, and 4, respectively, which are smaller than the experimental results (0.188, 0.192, and 0.172 mm, respectively). Similarly, the output power of each of the waves 1–4 also depends on the acceleration ratio. The maximum output power normalised by the area of the cantilever

was 1.2, 0.73, 0.77, and 0.62 nW·mm^{-2} for waves 1, 2, 3, and 4, respectively. The ratios of the output power for waves 2–4 do not correspond to the acceleration ratio as shown in Fig. 3.14.

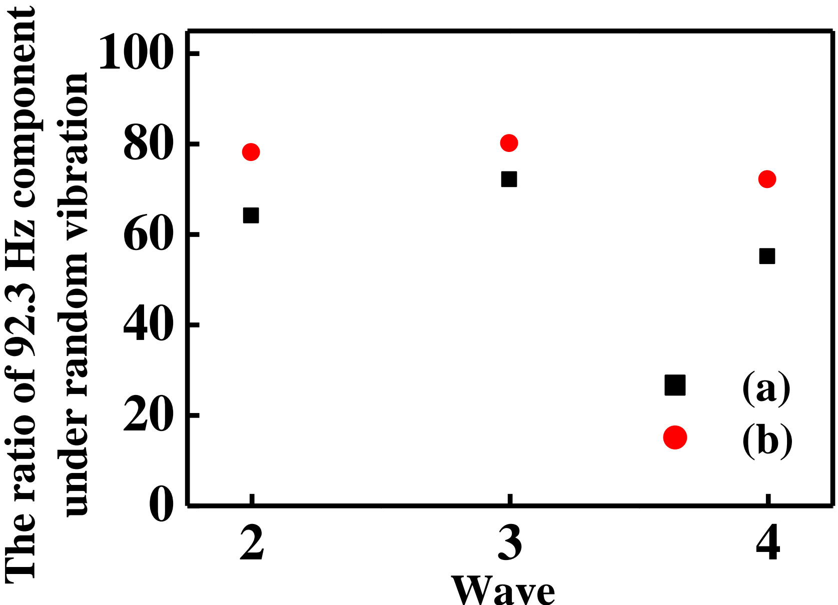

Fig. 3.14: The ratios of 92.3 Hz component on (a) acceleration and (b) output power under random vibration.

To investigate the effect of spurious component on output power in detail, the component of the output power at 92.3 Hz under wave 1-4 were characterized by the lock in amplifier. The results are shown in Fig. 3.14. The output power is independent of the wave. This indicates that the spurious component has no influence on the resonance response. The curves shown Fig. 3.15 have two regimes. For lower accelerations, the output power is proportional to the square of the acceleration. For higher accelerations, above 0.01 G, the output power is saturated because of nonlinear resonance. The incline of the curve at saturation gradually decreases with increasing acceleration. It appears

that this nonlinearity causes a difference in the acceleration and power or displacement ratio shown in Fig. 3.14.

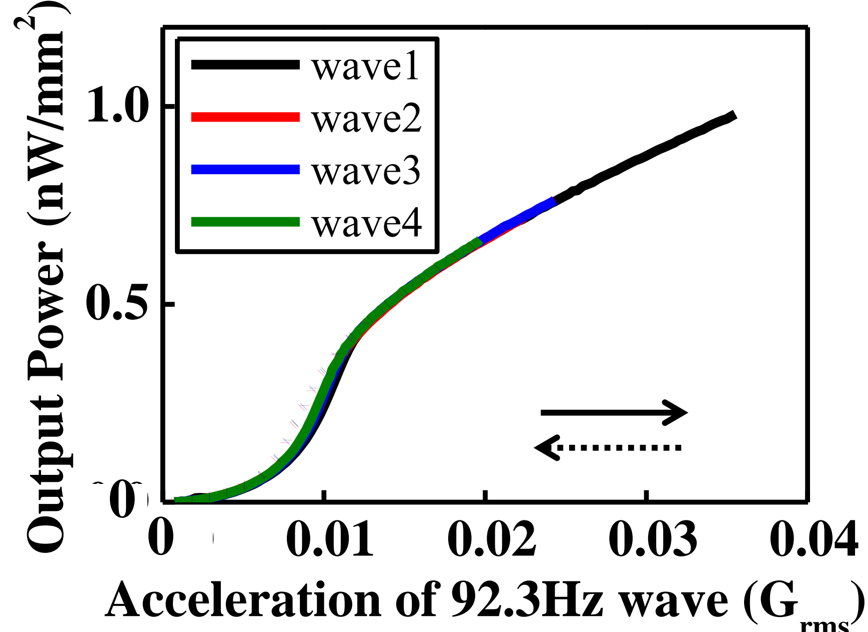

Fig. 3.15: Normalized output power as a function of acceleration of 92.3 Hz under (a) wave 1, (b) wave 2, (c) wave 3, and (d) wave 4.

3-4 Conclusions

Piezoelectric VEHs using MEMS technology were fabricated. To obtain better performance, (100)-oriented $BiFeO_3$ films on the (100)-oriented $LaNiO_3$ bottom electrode by the sol-gel method were prepared. The VEH with the low resonance frequency of ~100 Hz showed a high output power density of 7.6 $\mu Wmm^{-2}G^{-2}$ at a 1MΩ load resistance. It exceeded or was comparable to those of the best performing VEHs using other piezoelectric films. These results indicated that the (100)-oriented BFO film is a good candidate material for piezoelectric VEHs. Furthermore, from the Duffing

equation and Kirchhoff's law based governing equations, k_{31}^2= 4.3% was determined. Numerical calculated electromechanical properties showed the efficiency of experimental results against theoretical maximum generated power was approximately 70%. To achieve maximum performance of the VEHs, it was found that about 10% of k_{31}^2 is required.

Several waves composed of the fundamental (92.3 Hz), harmonic (184.6 Hz), and sub-harmonic (46.15 Hz) were also applied to the VEH to characterize electromechanical properties under random oscillations. The waveforms of displacement of the mass were independent of those of acceleration under ideal and random vibration and were only composed of a single frequency component corresponding to the resonance fundamental. In contrast, the displacement under random vibrations was smaller than that under ideal vibrations. To uncover its origin, the output power properties as a function of acceleration of the resonance frequency under ideal and random vibrations were characterized. The results were independent of the form of the vibration. This indicated that the decrease in displacement stems from the nonlinear resonance of the VEH and that the resonance response depends only on the fundamental component of the wave.

References

[1] K. Ujimoto, T. Yoshimura, A. Ashida, and N. Fujimura Appl. Phys. Lett. **100,** 102901 (2012).

[2] T. Yoshimura, K. Ujimoto, Y. Kawahara, K. Wakazono, K. Kariya, N. Fujimura, and S. Murakami, Jpn. J. Appl. Phys. **52,** 09KA03 (2013).

[3] K. Ujimoto, Ph. D. Dissertation in Osaka Prefecture University.

[4] K. Kariya, T. Yoshimura, S. Murakami, and N. Fujimura, Jpn. J. Appl. Phys. **53**, 08NB02 (2014).

[5] K. Kariya, T. Yoshimura, S. Murakami, and N. Fujimura, Jpn. J. Appl. Phys. **53**, 09PA14 (2014).

[6] Yoshimura T, Murakami S, Wakazono K, Kariya K and Fujimura N 2013 Appl. Phys. Exp. **6** 051501.

[7] Kim S G, Priya S, and Kanno I 2012 MRS Bull. **37**, 1039.

[3] N.H. Hagood, A. von Flotow, J. Sound Vibr. **146** (1991) 243.

[9] M .Renaud, K. Karakaya, T. Sterken, P. Fiorini, C. Van Hoof, R. Puers, Sens. Actu. A **145** (2008) 380.

Chapter 4: Nanoscale Probing of Direct Piezoelectric Response of $BiFeO_3$ Films by Scanning Probe Microscopy

4-1 Introduction

Chapter 2 indicates the control of not only growth orientation but also domain structure of $BiFeO_3$ films is quite important to enhance the electromechanical coupling properties (k_{31}^2). Moreover, it is found that there is no significant relationship between $e_{31,f}$ determined by the direct piezoelectric response and $d_{33(AFM)}$ of $BiFeO_3$ films (Appendix, Fig. A1). Although it was reported that $d_{33(AFM)}$ is easily influenced by several contributions such as the electrostrictive and charging effects [1,2], it appears that the direct piezoelectric response of $BiFeO_3$ films contains the domain wall contribution. This is because $d_{33(AFM)}$ is mainly dominated by the intrinsic contribution whereas the $e_{31,f}$ by the direct piezoelectric response contains all the piezoelectric response. However, the direct evidence of domain wall contribution to the direct piezoresponse could not be obtained.

To investigate the domain wall contribution on the direct piezoelectric response, it needs to measure the direct piezoelectric response at the domain walls. Although Genevrier et al. have reported that the measurement of direct piezoelectric response by scanning probe microscopy, the spatial resolution and sensitivity are insufficient for this purpose [3]. In this article, we demonstrate the observation of ferroelectric domain structure of $BiFeO_3$ films at high resolution and quantitative measurement of the effective longitudinal piezoelectric coefficient by using direct piezoelectric response microscopy (DPRM). Then by combining the analysis of conventional PFM, we discuss

the enhancement of the direct piezoelectric response at the domain walls and how to obtain the k_{31}^2 required for the application of VEHs, which is calculated in chapter 3.

4-2 Experiment Procedure

4-2-1 Set-up for Nanoscale Characterization of Direct Piezoresponse (DPRM)

An SPM (SII NanoNAvi) was modified to observe the direct piezoresponse of a nanoscopic region. A schematic illustration of DPRM is shown in Fig. 4.1. To apply a modulated mechanical force to a sample, a piezoelectric actuator was placed on the sample stage of the SPM. The sample was set on the actuator. A conductive AFM probe was contacted to the sample surface and then the actuator was operated at a higher frequency than the cutoff frequency of the low-pass filter within the feedback controller of SPM, which avoided the cancellation of the applied force by the z-feedback control and maintained a constant contact of the cantilever with the sample surface. The schematic of the operation of DPRM is shown in Fig. 4.2. In DPRM, local modulated compressive force is applied to a sample from the conductive cantilever by the vibration of the actuator and then the induced direct piezoresponse is detected by using lock-in-amplifier. The ferroelectric domain images are obtained by measuring direct piezoresponse while scanning the specific area under constant force modulation.

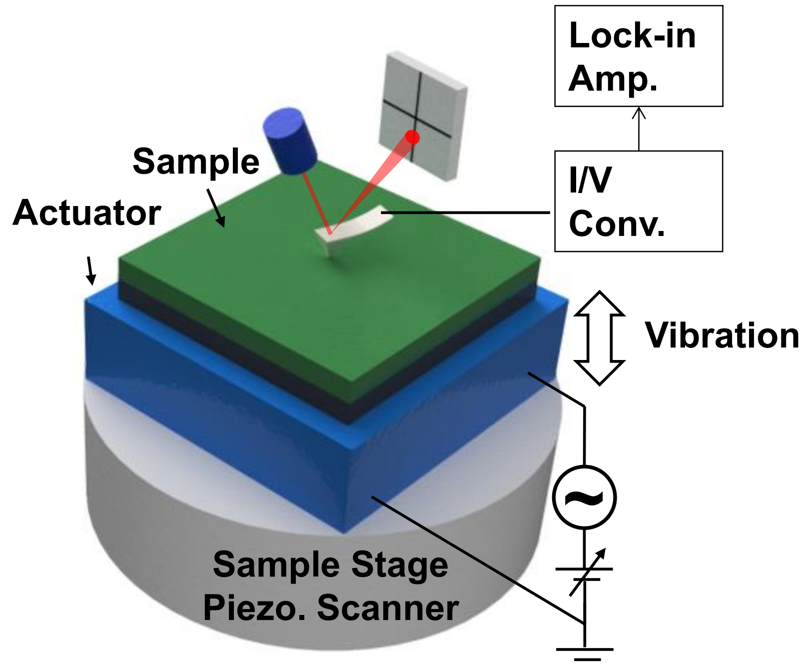

Fig. 4.1: **Direct piezoelectric response microscopy (DPRM) technique.** Schematic illustration of the experimental set-up for DPRM.

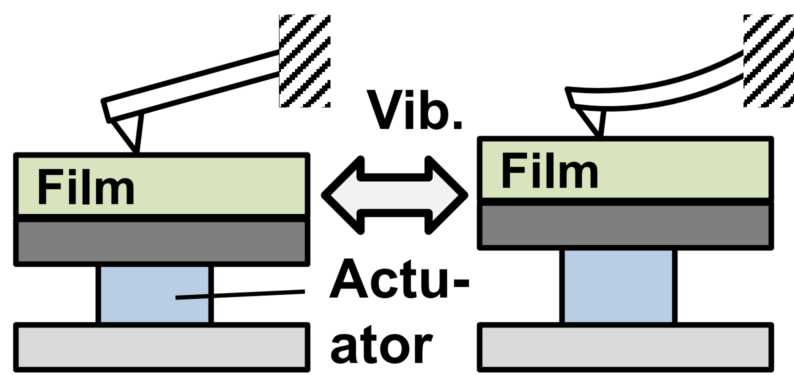

Fig. 4.2: Nanoscale moderated stress applied from cantilever by the vibration of actuator. Schematic illustration of the operation of DPRM.

4-2-2 Detailed Measurement Method and Condition for Accurate DPRM Measurement

Figure 4.3(a) shows the schematic diagram of DPRM on the peripheral of contact area. When a conductive cantilever is attached to a film, a parasitic capacitance of more than 10^{-12} F, which is much higher than the sample capacitance (below 10^{-19} F in the case of $BiFeO_3$ film) is formed between the conductive cantilever beam and the bottom electrode of the sample In DPRM, it is a critical problem because it leads to underestimate the generated voltage by direct piezoelectric effect as shown in Fig. 4.3(b). On the other hand, it has little effect on the generated current. Therefore, to avoid the effect of this parasitic capacitance, an I/V converter was used. The equivalent of this measurement is shown in Fig. 4.3(c). R_i and C_i of the I/V converter were 1.0 MΩ and 3.3 pF, respectively. Ideally, the output current (I_p) is proportional to the frequency of the applied force, because the induced charge via the direct piezoelectric effect is proportional to the force and the output current is given by the charge differentiation. Given that the cutoff frequency of the I/V converter, which is 10 kHz as shown in Fig. 4.3(d), all the measurements were carried out at below 10 kHz. Besides since the I_p is also proportional to the amplitude of the applied force, the cantilever with relatively large bulk modulus was selected.

Based on the discussion above, the detailed condition of DPRM was determined. In this thesis, a commercially available conductive Pt/Cr-coated AFM probe (Budget Sensors: ElectriTap190) with a radius of 25 nm and spring constant of 48 N/m was attached to a film sample. The sample was vibrated along the longitudinal axis by a laminated piezoelectric actuator that was operated by an nf-function generator

(WF1965). Periodic compressive strain was applied to the film at a frequency of 7.3 kHz. The charge induced via the direct piezoelectric response was measured using a lock-in amplifier (NF LI5640). Ferroelectric domain images were obtained by measuring the direct piezoresponse while scanning a specific area under constant force modulation.

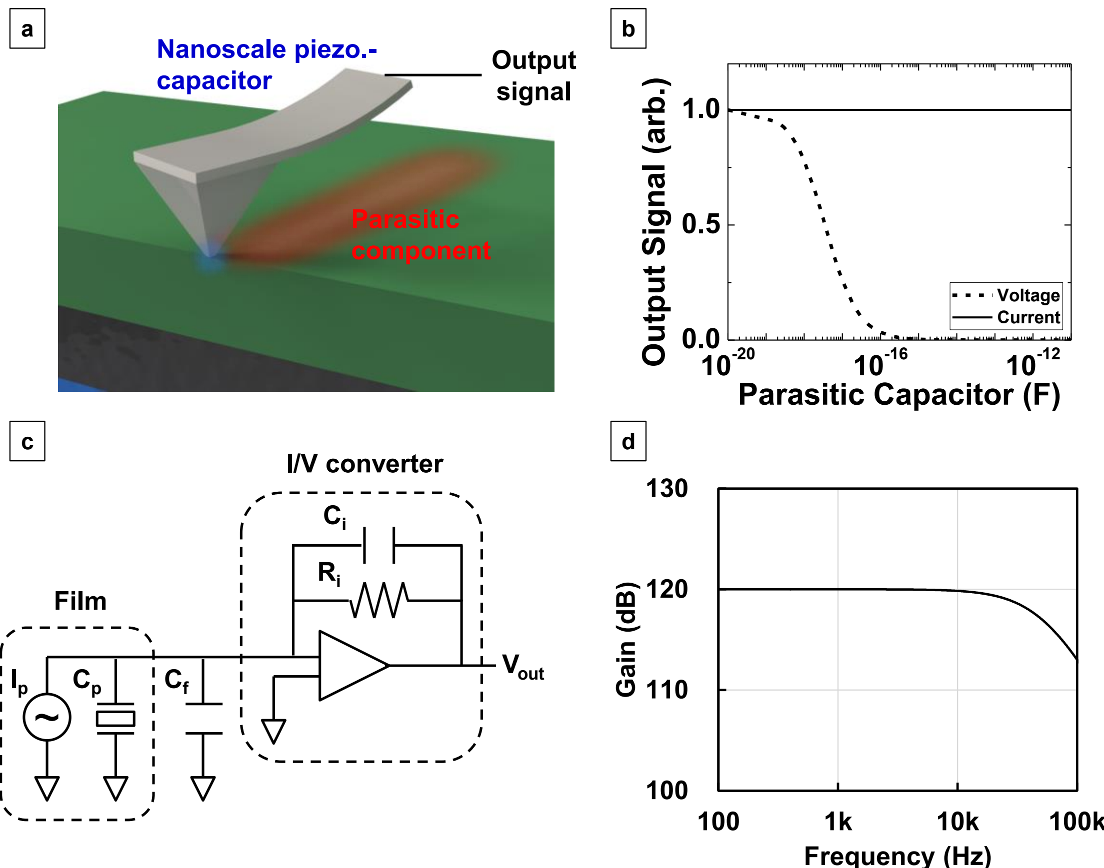

Fig. 4.3: **Piezoelectric current detection by the I/V converter. a.** Schematic diagram of DPRM on the peripheral of contact area. **b.** Output voltage (dotted line) and current (solid line), generated by direct piezoelectric effect, dependence of parasitic capacitance formed between the cantilever beam and the sample. **c.** Equivalent circuit when a cantilever is attached to the surface of the sample. The induced piezoelectric current is detected by the I/V converter. **d.** Dependence of frequency on gain.

4-2-3 Finite Element Simulated Electromechanical Properties of DPRM

In order to perform the accurate DPRM measurement, it is imperative to understand how the local force is transmitted to the piezoelectric film. The output signal of DPRM was analysed by the finite element method (Femtet, Murata Software Co., Ltd., Tokyo, Japan). In the simulations, a force (F) was applied from the AFM tip to the piezoelectric film. Figure 4.4(a) shows the stress and surface deformation in the out-of-plane direction. The analysis was carried out with an F of 1 μN; tip diameter (D) of 20 nm; and thickness (h), Young's modulus (E) and d_{33} of the piezoelectric film of 200 nm, 73 GPa, and 245 pm/V, respectively. The stress was distributed in the film, and the surface around the tip was deformed. Figure 4.4(b) displays the relationship between the induced charge (Q) via the direct piezoelectric response and F under the same conditions as in Fig. 4.4(a). We found that Q increased linearly with F and that the proportional relationship was simply given by $Q = d_{33}F$ despite the application of uneven stress. Moreover, this relationship was almost valid under other conditions, as illustrated in Fig. 4.4(c). In this analysis, D and h were varied from 20 to 100 nm and from 20 to 500 nm, respectively. The charges were almost independent of D and h, which suggests that DPRM can achieve quantitative analysis regardless of the measurement conditions and sample structure. Moreover, the direct piezoelectric response was hardly influenced by other contributions such as the electrostrictive and charging effects, because no electric field was applied in the measurement [1,2]. Therefore, DRPM should have the ability to measure the pure piezoelectric response of ultrathin piezoelectric films, which is an advantage over conventional PFM.

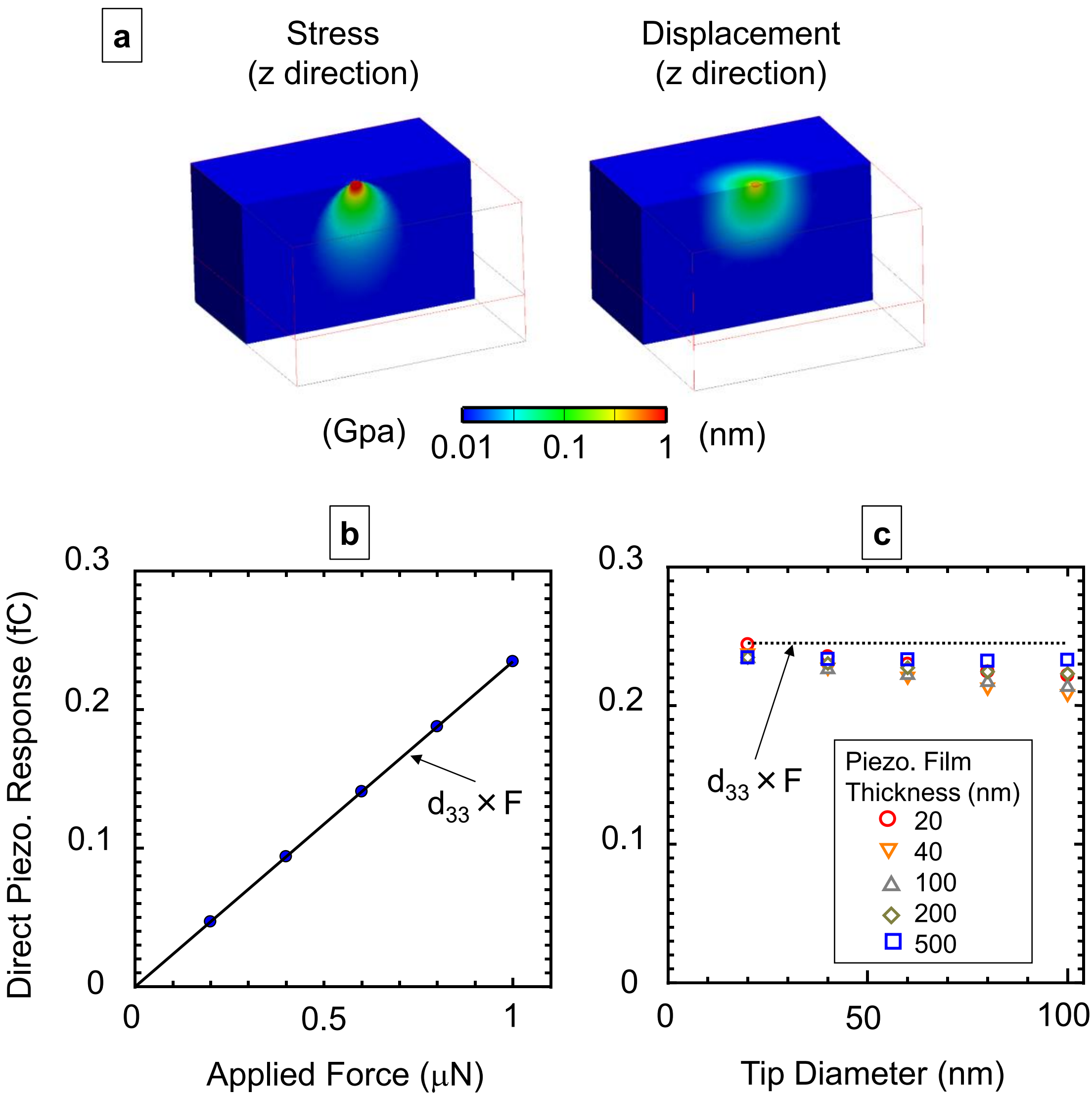

Fig. 4.4: **Finite element analysis for DPRM. a,** stress(left) and surface deformation (right) along z direction. Dependence of the direct piezoelectric response via the cantilever on **b,** applied mechanical force and **c,** thickness of the piezoelectric film and the diameter of the SPM tip.

4-2-4 Preparation of Measurement Samples

The samples consisted of (100) and (111) $BiFeO_3$ epitaxial thin films grown on

(100) $SrRuO_3$/(100) $SrTiO_3$ and (111) $SrRuO_3$/(111) $SrTiO_3$ substrates, respectively, using pulsed laser deposition. X-ray reciprocal space mapping indicated that both films had rhombohedral structure. The macroscopic remnant polarisation of (111) and (100) films was 95 and 56 μC/cm^2, respectively, and their $e_{31,f}$ values were −1.3 and −3.1 C/m^2, respectively [4].

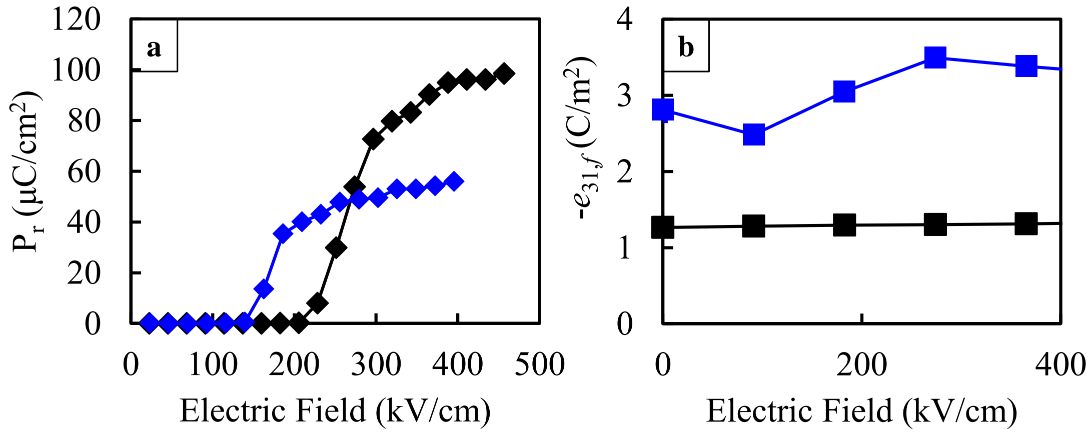

Fig. 4.5: **Ferroelectric and piezoelectric properties of $BiFeO_3$ films. a.** Ferroelectric properties. **b.** Piezoelectric properties. Blue and black lines and marks are the results of (111) and (100) epitaxial $BiFeO_3$ film.

4-3 Results and discussion

4-3-1 Demonstration of DPRM

Based on above described concepts, a prototype 1 of DPRM was prepared and demonstrated. The schematic is illustrated in Fig. 4.6(a). In the prototype 1, the actuator, pasted on a stage, was simply placed and fixed under a sample holder. (100) $BiFeO_3$ epitaxial film was used as the measurement sample. Figure 4.6(b) shows the $I_0 \sin\theta$, which I_0 is detected current, obtained by modulated force of 3 μN at the frequency of 6.4 kHz. As can be seen, the S/N is much low. Besides the calculated piezoelectric

coefficient is too large ($d_{33,f}$~1000) for ferroelectric thin films. Therefore, it is considered that this detected signal is not piezoelectric response. Figure 4.7 shows the detected current dependence of the applied voltage of the actuator. In Fig. 4.7 the current was measured at the condition when the cantilever was attached to the sample and there is 10μm distance between the tip of cantilever and the sample. As can be seen, almost same current is detected at the both condition. From these results, it is concluded that electromagnetic wave from the actuator cause these problems.

Thus, the Cu based electromagnetic interference shield was prepared and attached to the actuator. The schematic illustration of the prototype 2 is shown in Fig. 4.8(a). The attached shield was made by hand. Figure 4.8(b) also shows the $I_p \sin\theta$. Interestingly, the obtained image is quite different from the result of the prototype 1 (Fig. 4.7) and obvious domain image with high S/N could be obtained. The amplitude of detected current was also reasonable. The details of the amplitude and quantitatively of the detected piezoresponse are described below sections.

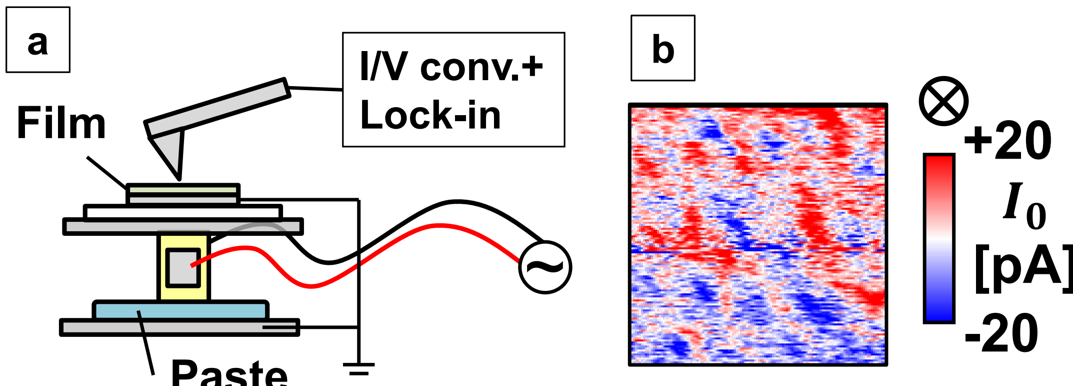

Fig. 4.6: **DPRM demonstration using prototype 1. a.** Schematic of prototype 1. **b.** the detected current mapping image.

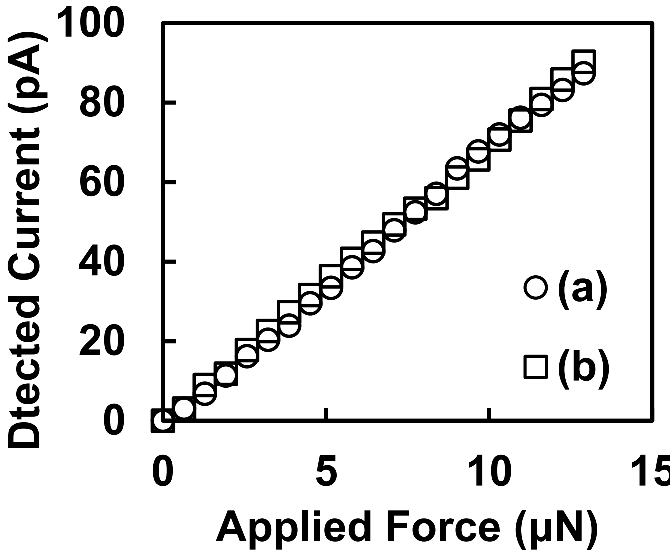

Fig. 4.7: **Effect on electromagnetic wave from the actuator.** Detected current dependence of the applied modulated force at 6.4 kHz on two conditions: (a) the cantilever is attached onto the sample surface and (b) there is 10μm sample-tip distance.

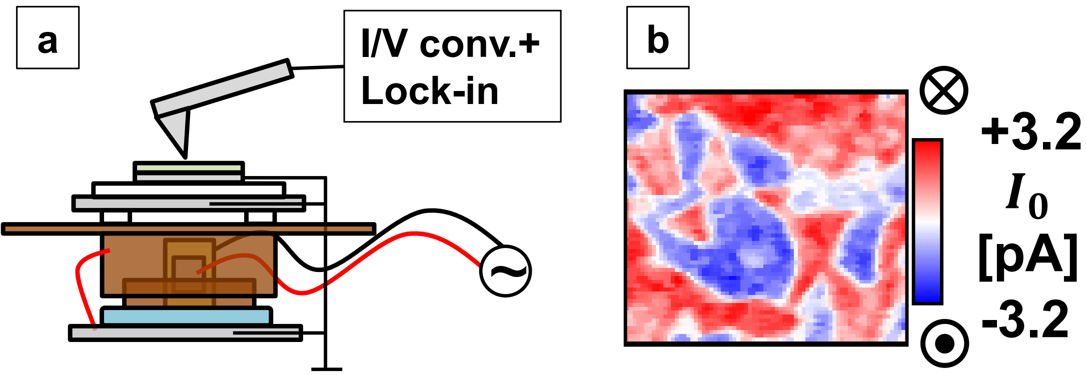

Fig. 4.8: **DPRM demonstration using prototype 2. a.** Schematic of prototype 1. **b.** the detected piezocurrent mapping image. The regions of red and blue show downward and upward polarization domain, respectively.

Finally, the electromagnetic interference shield shown in Fig. 4.9 was designed and prepared. To decay the effect on electromagnetic wave as much as possible, the peripheral of the actuator is covered by the shield. The prototype 3 is be assembled by

the one parts pasted to the top of actuator, which the bottom is pasted to another parts. The sample holder was attached onto the assembled prototype 3 as shown in Fig. 4.10 and then it was placed on the SPM system. The peripheral of DPRM system was also grounded completely.

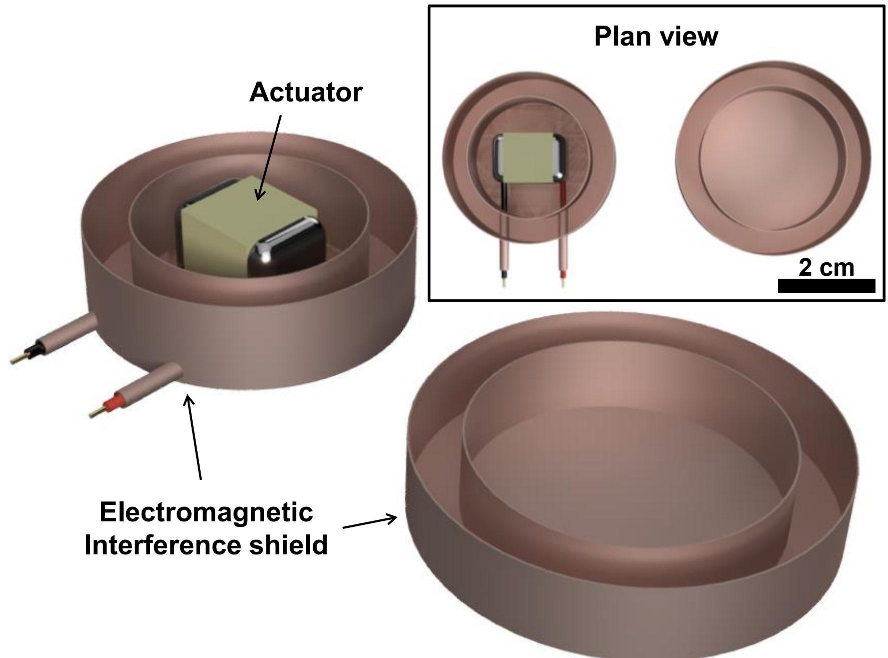

Fig. 4.9: **Designed shield box for DPRM.** The total size of prototype 3 is radius ≅ 1.0 cm and height ≅ 0.54 cm.

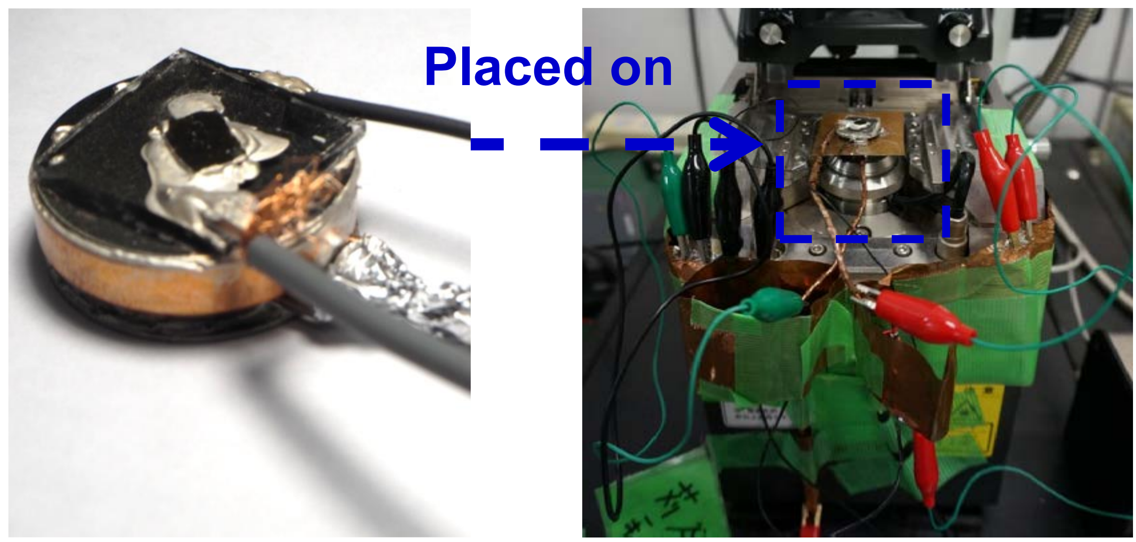

Fig. 4.10: **Assembled DPRM system.** Photo of DPRM system.

4-3-2 Observation of Domain Structure Using Direct Piezoelectric Effect

Figure 4.11(a) shows a topographic image obtained by DPRM for the (100) $BiFeO_3$ film. Compressive force modulation of 1300 nN was applied. The topographic DPRM image was almost identical to that of conventional SPM, which indicates that the sinusoidally applied force did not influence the observation of topology and the constant contact of the AFM probe with the sample was maintained. Figure 4.11(b) depicts the corresponding phase image of DPRM, which maps the phase difference between the applied force and direct piezoelectric response. The phase signals (θ) of 90° and −90° correspond to upward and downward domains, respectively. The domain pattern was clearly observed by DPRM. The obtained pattern is almost identical to the PFM phase image shown in Fig. 4.11(c). The histograms of the phase signals for DPRM and PFM in Fig. 4.11(d) indicate that DPRM has almost same spatial resolution as that of PFM. The phase difference of 180° between the upward and downward domains

indicates that the signal originates primarily from the direct piezoelectric response. In contrast to this result, Gruverman et al. reported that the polarisation switching was induced by the application of the strain gradient generated by SPM tip [5]. Although the measurement method was similar to that of DPRM, such phenomena were not observed, as shown in Supplementary Fig. A3, in which direct piezoresponse mapping images were obtained under force modulation of 600–2300 μN. It seems that the difference between their experiment and DPRM is the electrical conditions of the AFM probe. In DPRM, no electric field is applied to the film because the imaginary short circuit is formed by the I/V converter.

Figure 4.12(a) and (c) show the DPRM and PFM amplitude images, respectively. These images indicate that the signal-to-noise ratio of DPRM was comparable to that of PFM. While the domain patterns are almost the same in these two images, the amplitude distributions differ. The domains with large direct piezoelectric response indicated in Fig. 4.12(a) have small converse piezoelectric response in Fig. 4.12(c). Thus, the direct and converse piezoelectric responses have different active regions. This result is consistent with a previous comparison of direct and converse piezoresponses[19].

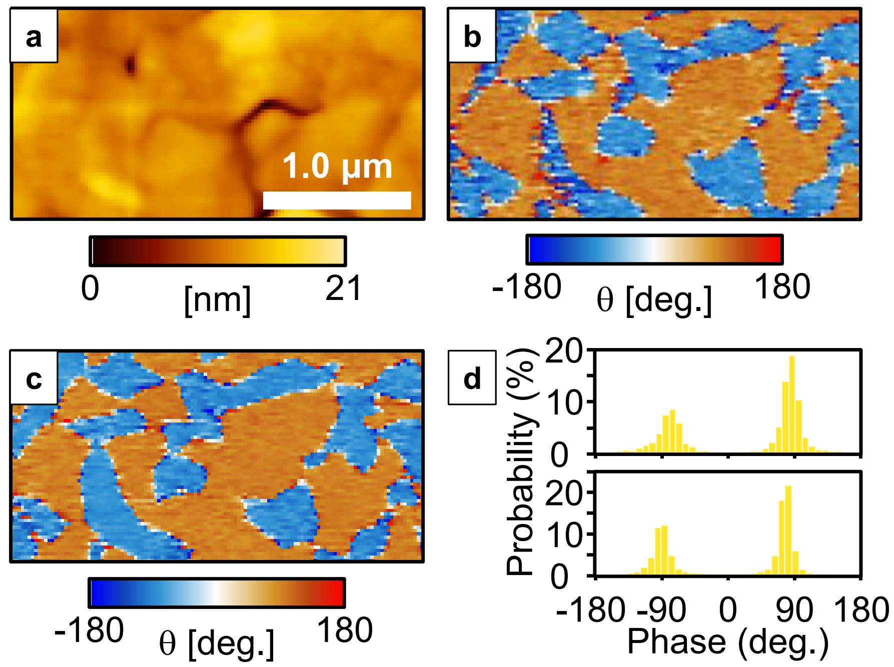

Fig. 4.11: **DPRM measurement of a (100) $BiFeO_3$ epitaxial film. a,** Surface morphology of the film. Phase images obtained by **b,** DPRM and **c,** PFM. **d,** Frequency spectrum of the phase image obtained by DPRM (top) and PFM (bottom).

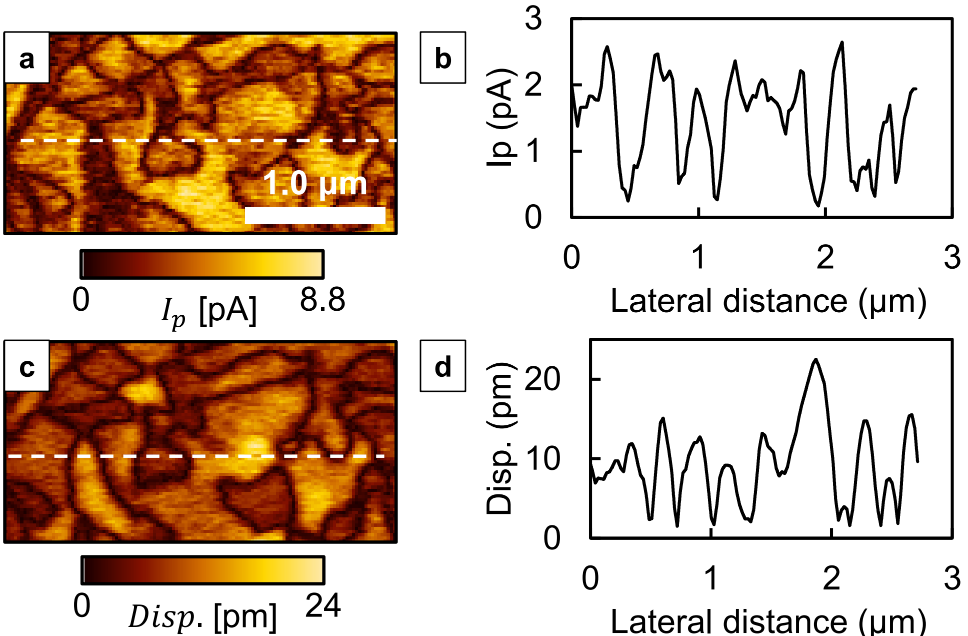

Fig. 4.12: **Comparison of mapping images obtained by DPRM and PFM.** Absolute **a,** DPRM and **b,** PFM mapping results. **c, d** Cross-sectional images on the lines depicted in **a** and **b,** respectively.

4-2-3 Quantitative Analysis of Contribution of Domain structure on Direct Piezoresponse of $BiFeO_3$ Films

The contribution of the domain walls to the direct piezoelectric response of the $BiFeO_3$ films was investigated by combining the PFM and DPRM measurements. Figure 4.13(a) shows the domain structure of the (111) film measured by PFM. The (111) film had a single domain structure with downward spontaneous polarisation; domain walls were not observed. Figure 4.13(b) shows the domain structure of the (100) film determined from the vertical and lateral PFM images. The details of the determination are provided in Supplementary Fig. A3. The (100) film has a multidomain structure composed of 71° and 109° domain walls. The DPRM images of the $I_p\sin\theta$

signal of the (111) and (100) films are presented in Fig. 4.13(c) and (d), respectively. The (111) film shows a homogeneous distribution of the signal, which is consistent with the results shown in Fig. 4.13(a) and the quantitative analysis ability of DPRM discussed above. In contrast, the (100) film exhibits a large distribution of the amplitude of I_p. To investigate the origin of this distribution in detail, $e_{33,f}$ was calculated using

$$e_{33,f} = d_{33}E = \frac{EI_p}{2\pi fkx} \tag{1}$$

where k is the spring constant of the AFM probe and f and x are the operating frequency and displacement of the actuator, respectively. The $BiFeO_3$ films were assumed to have E = 170 GPa. The cross sections of $e_{33,f}$ distribution for the (111) and (100) films are shown in Fig. 4.13(e) and (f), respectively. The areas inside the dashed black rectangles in Fig. 4.13(a) and (b) were used for this calculation. From Fig. 4.13(e), the average $e_{33,f}$ is calculated to be 2.7 C/m^2, which corresponds to the intrinsic piezoelectric response of the (111) film because this film has a single domain structure (denoted domain A). In contrast, the (100) film has different $e_{33,f}$ values depending on the domain, as shown in Fig. 4.13(f). The domain surrounded by 109° domain walls (denoted domain B) has an average $e_{33,f}$ of 5.7 C/m^2. The domain with 71° domain walls (denoted domain C) has an average $e_{33,f}$ of 7.3 C/m^2, which is 30% larger than that of domain B. The difference between the $e_{33,f}$ values of domain A and domain B originates from the domain engineered configuration, because the $BiFeO_3$ films used in this study have rhombohedral structure. The increase of $e_{33,f}$ in domain C of 1.6 C/m^2 indicates the contribution of the 71° domain walls to the direct piezoelectric response. This enhancement is not caused by the difference of the spontaneous polarisation direction,

because domain D, which has the same spontaneous polarisation direction as that of domain C and no 71° domain walls, has smaller $e_{33,f}$ than that of domain C. Moreover, the 71° domain walls are tilted with respect to the film surface. It appears that this tilt contributed to the increase of $e_{33,f}$ in the peripheral area of the 71° domain walls. The maximum $e_{33,f}$ was observed in the region where the 71° domain walls overlapped. This also supports the domain wall contribution to the piezoresponse of domain-engineered ferroelectrics reported by Wada and colleagues[5]. The enhancement of the direct piezoelectric response at the 71° domain wall can be explained by the broadening of the domain walls induced by the stimulus, as proposed by Rao and Wang [6,7].

Finally, the contribution of the 71° domain walls to the macroscopic direct piezoelectric response characterised by $e_{31,f}$ is discussed. For the (111) film, which has only an intrinsic contribution, the ratio of $e_{31,f}$ (=−1.3 C/m^2) to $e_{33,f}$ (=2.7 C/m^2) is −2.1. By applying this ratio to $e_{33,f}$ of domain B (5.7 C/m^2), the estimated intrinsic contribution of $e_{31,f}$ of the (100) film is −2.7 C/m^2. The difference between the measured $e_{31,f}$ (=−3.5 C/m^2) and intrinsic contribution of $e_{31,f}$ is −0.8 C/m^2, which corresponds to the contribution of the 71° domain walls. This value is consistent with that estimated from the enhancement of $e_{33,f}$ caused by the contribution of the 71° domain walls, which is 1.6 C/m^2. Because the 71° domain walls are mainly formed between domains with the spontaneous polarisation in the same out-of-plane direction, the 71° domain walls will remain after the poling treatment and can contribute the enhancement of the direct piezoelectric response. Although the domain wall contribution to the direct piezoelectric response of the $BiFeO_3$ films is only 30% of the intrinsic contribution, it is important for energy conversion applications such as energy harvesting, because the

electromechanical coupling factor (k^2) is proportional to the square of the piezoelectric coefficient. It is estimated that almost half of k^2 originates from the domain wall contribution.

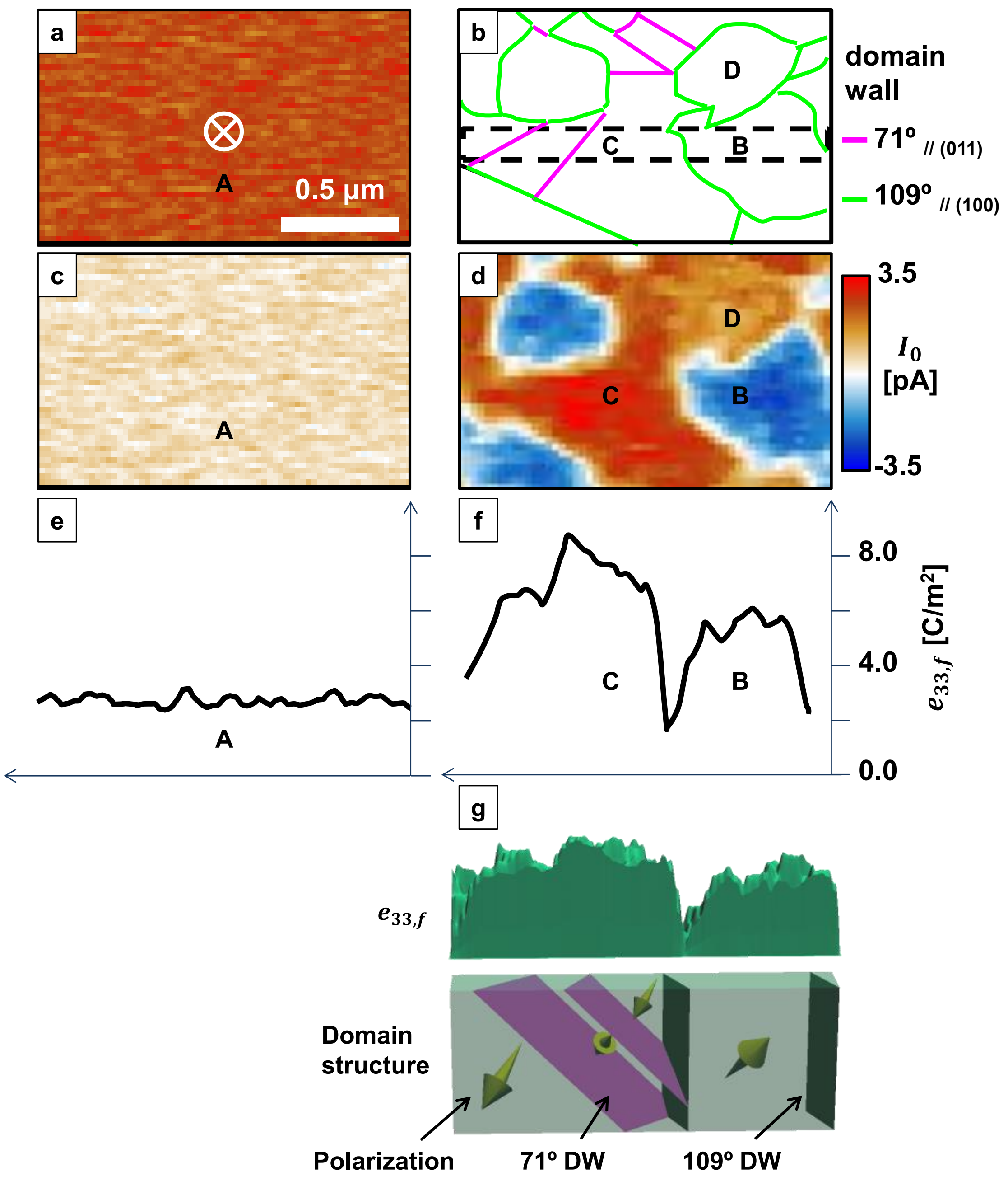

Fig. 4.13: **Local piezoresponse of (111) (left side) and (100) BiFeO3 epitaxial films (right side). a, b,** Domain structure determined by the converse piezoelectric effect. **c, d,** Direct piezoresponse mapping images. **e, f,** Average $e_{33,f}$ cross-section at the area surrounded by the black dotted line. blue, green, and orange regions in Fig. (f) show the amplitude of the intrinsic, domain engineering, and domain wall contributions, respectively.

4-4 Conclusions

This work presents a technique to observe the ferroelectric domain structure by direct piezoelectric effect and to characterize the effective longitudinal piezoelectric coefficient quantitatively. It was found that the significant increase of the direct piezoelectric response in the domains with 71° domain walls. This work should stimulate the approach to enhance the piezoelectric properties by the modification of the domain structure including the introduction of the domain walls.

Method

The current induced via the direct piezoresponse is described as $I_p \sin(\omega t + \theta)$, where I_p is the amplitude of the induced current, ω is angular velocity, t is time and θ is phase. Therefore, the electric displacement component (D_3) can be derived from

$$D_3 = \int_0^t \frac{I_p}{A} \sin(2\pi f t + \theta) dt = -\frac{I_p}{2\pi f A} \cos(2\pi f t + \theta), \quad \text{(M.1)}$$

where A is the contact area of the tip. Using the piezoelectric constitutive equations

$$D_i = d_{ij,} T_j + \varepsilon_{ik}^T E_k \quad \text{(M.2)}$$

$$= e_{ij,} S_j + \varepsilon_{ik}^S E_k \quad \text{(M.3)}$$

$i,k = 1,2,3 \qquad j = 1,2,\ldots,6$

where Sij is strain, ε_{ik}^S is the electrical permittivity under constant strain and E_k is electric field, $e_{33,f}$ can be written as

$$e_{33,f} = \frac{I_p}{2\pi f A \varepsilon_{33}} \quad \text{(M.4)}$$

The strain applied to the film was calculated by

$$\varepsilon_{33} = \frac{kx}{AE} \quad \text{(M.5)}$$

The equation used to calculate $e_{33,f}$ (Equation (1)) was obtained from Equation (M.4) and (M.5).

The mapping measurement of PFM was carried out by applying an AC voltage of 1.0 V_{rms}. The eight equivalent directions for polarization vector in the (100) epitaxial film were visualised by rotating the sample in −55° increments around the (010) plane and combination of the out-of-plane and in-plane converse piezoelectric responses. The details are described in Supplementary Fig. A2.

References

[1] Vasudevan. R. K. *et al.* Mesoscopic harmonic mapping of electromechanical response in a relaxor ferroelectric. *Appl. Phys. Lett.* **106,** 222901 (2015).

[2] Balke. N. *et al.* Exploring Local Electrostatic Effects with Scanning Probe Microscopy: Implicatiions for Piezoresponse Force Microscopy and Triboelectricity. *ACS Nano* **8,** 10229-10236 (2014).

[3] Gomez. A. *et al.* Piezo-generated charge mapping revealed through direct piezoelectric force microscopy. *Nat.commun.* **8,** 1113 (2017).

[4] Ujimoto, K. *et al*. Direct piezoelectric properties of (100) and (111) $BiFeO_3$ epitaxial thin films. *Appl. Phys. Lett.* **100**, 102901 (2012).

[5] Lu. H. *et al.* Mechanical Writing of Ferroelectric Polarization. *Science* **336,** 59-61 (2012).

[6] Wada. S. *et al.* Enhanced piezoelectric properties of barium titanate single crystals with different engineered-domain sizes. *J. Appl. Phys.* **98,** 014109 (2005).

[7] Rao. W.& Wang. Y. U. Domain wall broadening mechanism for domain size effect of enhanced piezoelectricity in crystallographically engineered ferroelectric single crystals. *Appl. Phys. Lett.* **90,** 041915 (2007).

Appendix of Chapter 4

Macroscopic $e_{31,f}$ vs. nanoscopic $d_{33,AFM}$

The macroscopic $e_{31,f}$ and nanoscopic $d_{33,AFM}$ coefficients were characterized for $BiFeO_3$ oriented and epitaxial films[1-4] prepared at various conditions and methods. Former is measured by substrate bending and collecting developed charges method and the latter is determined from the strain curve obtained by PFM. The results are summarized in Fig. A1. As can be seen, no significant relationship between each piezoresponse is observed.

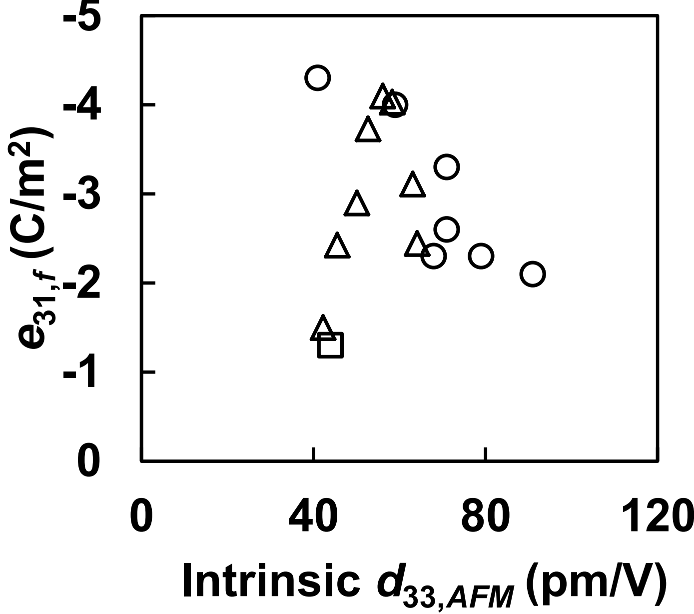

Fig. A1: **Intrinsic $d_{33,AFM}$ coefficients dependence on macroscopic $e_{31,f}$ coefficient.** Circle, square, and triangle mark show the data of (100) epitaxial, (111) epitaxial, and (100) oriented $BiFeO_3$ films.

Determination of domain walls by CPRM

Piezoelectric force microscopy was used for determination of the types of the

domain walls[5]. To distinguish four variants of the in-plane direction of the spontaneous polarization, the angle between the direction of the cantilever beam and <100> of $BiFeO_3$ was set at 55°. The schematic illustration of the measurement is shown in Fig. A2(a). The out-of-plane and in-plane directions of the spontaneous polarization are determined by the vertical and lateral PFM measurements, respectively, as shown in Fig. A2(b) and A2(c). Figure A2(d) and A2(e) show the results of vertical and lateral PFM measurements for the (100) $BiFeO_3$ epitaxial film. From these results, the directions of the spontaneous polarization for each domain were determined as shown in Fig. A2(f). From the relationship between the directions of the spontaneous polarization in the adjacent domains, the type of the domain walls, which are 71°, 109°, and 180° domain walls, were determined as shown in Fig. 4.13(b).

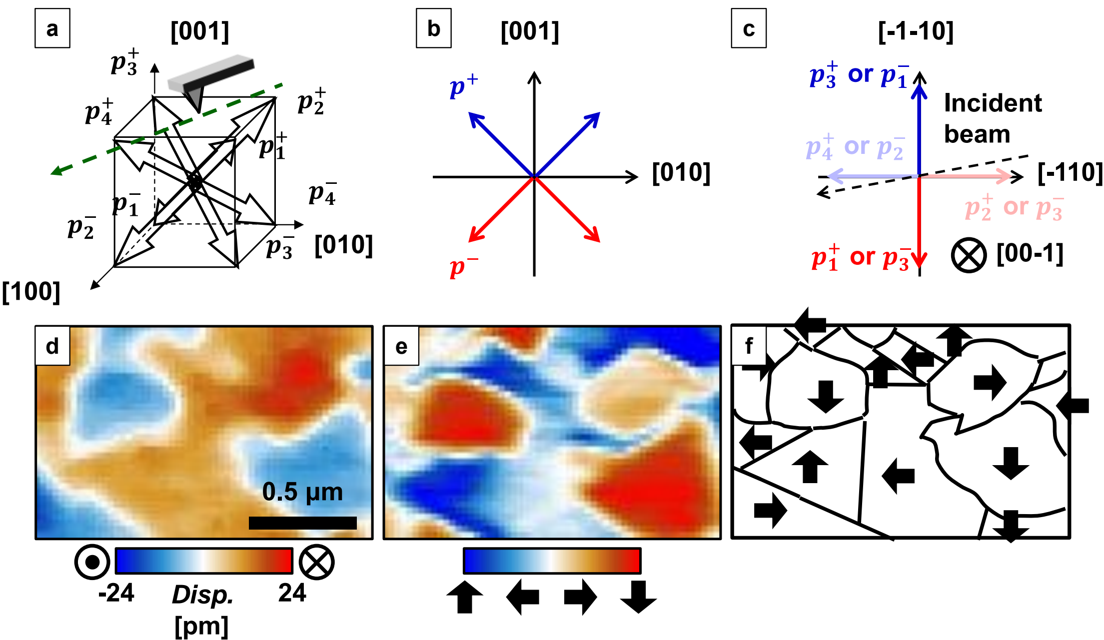

Fig. A2: **Domain wall detection by PFM. a,** Schematic figure of dipole vectors in unit-cell. The relationship between detected signals and depicted color in **b,** vertical and **c,** lateral converse piezoresponse. The **d,** vertical and **e,** lateral domain pattern image of (100) $BiFeO_3$ epitaxial film obtained by PFM measurement. **f,** The visualized lateral domain vector image of the film.

DPRM mapping images dependence on compressive force

DPRM measurements were carried out at the compressive mechanical force modulation from 600 to 2300 nN. Figure A3a-h shows the morphology and the direct piezoelectric response of the (100) $BiFeO_3$ film measured at various force. As can be seen, all the mapping images have similar pattern. Although it appears that the $e_{33,f}$ coefficient decreases when the applied force is more than 1300 nN, the change of the domain structure including the polarization switching is not observed.

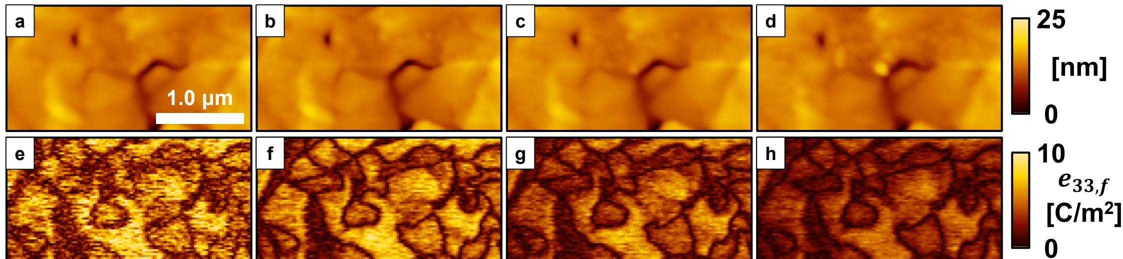

Fig. A3: **Change of the topography (upper side) and piezoresponse (bottom side) of (100) $BiFeO_3$ epitaxial film on the increase of mechanical compressive force modulation.** The images at the force of **a,c** 600 nN, **b,f,** 1300nN, **c,g,** 1600 nN, and **d,h** 2300 nN.

Chapter 5: Summary

This thesis has been devoted to the study on “”Nanoscale Probing of Direct Piezoelectric Properties and Vibration Energy Harvesting Application of $BiFeO_3$ Films ”. The main results of this work can be summarized as follows.

In Chapter 2, to improve the piezoelectric properties of sol-gel-derived $BiFeO_3$ films for MEMS VEHs application, (100) oriented films were prepared by using $LaNiO_3$ bottom electrodes, which have preferential (100) orientation on Si substrates. From the comparison between microstructure and direct piezoresponse at macroscopic region, it was found that domain size and tensile stress, applied to the (100) orientated $BiFeO_3$ films, enhanced the electromechanical properties of the $BiFeO_3$ films.

In Chapter 3, electromechanical properties of VEHs with the $BiFeO_3$ films were characterized. By controlling the growth orientation of $BiFeO_3$ films, the output power was enhanced significantly, compared to the VEHs using polycrystalline $BiFeO_3$ films. From the results of numerical calculation using the physical values exerted from the fundamental characterization of the VEHs, it was clarified that the performance of the fabricated VEHs and the required k_{31}^2 for the application of VEHs were 70% of the theoretical limit and 10%. These results indicate that full potential of the VEHs can be delivered by improving the electromechanical properties of $BiFeO_3$ films and it can be comparable with the $Pb(Zr,Ti)O_3$ films.

In Chapter 4, Scanning probe microscopy based measurement technique for observing domain structure and nanoscopic direct piezoresponse, utilizing direct piezoelectric effect, was developed. Chapter 2 and 3 indicated that it was imperative to

characterize the nanoscopic direct piezoresponse to enhance the k_{31}^2 of $BiFeO_3$ films and achieve the maximum performance of the VEHs. From the DPRM mapping results, it was found that DPRM could observe obvious domain structure, which is almost same sensitivity with conventional piezoelectric response microscopy from converse piezoelectric effect. Moreover, it found interesting experimental results that the direct piezoresponse is enhanced at the vicinity of 71° domain wall and increase of the density is effective to improve the direct piezoresponse. Combining the developed and conventional microscopy technique, the amplitude of intrinsic, domain engineered configuration, and domain wall contribution to the $e_{31,f}$ of (100) $BiFeO_3$ epitaxial film are up to -0.7 and -2, and >-0.8 C/m^2. Although the domain wall contribution on the direct piezoelectric response of the $BiFeO_3$ films is only 30% of the intrinsic contribution, it has significant role on the energy conversion application such as energy harvesting, because the electoromechanical coupling factor (k^2) is propositional to the square of the piezoelectric coefficient. It can be estimated that almost half of k^2 is originated form the domain wall contribution.

Throughout these works, some designing principle of ferroelectric films for the application of VEHs could be established. In VEHs, k_{31}^2=10% is sufficient to achieve theoretical maximum electromechanical performance of the VEHs. Since direct piezoresponse also contains intrinsic and extrinsic contribution, the control of domain structure is important to obtain large k_{31}^2, especially in chapter 4, it is appeared that the nanoscopic direct piezoresponse is enhanced by the increase of 71° domain wall density. Although further works is needed, domain wall density might be a factor to enhance the direct piezoresponse as same as converse piezoresponse reported by Wada *et al.*.

These scientific knowledge is expected to lead the fabrication of lead-free piezoelectric films with large k_{31}^2, comparable with PZT, for VEHs.

Acknowledgement

The works summarized in this doctoral thesis were performed throughout the doctoral course in Physics of Novel Devices Laboratory at Osaka Prefecture University.

I would like to express my gratitude to Professor Norifumi Fujimura for his valuable guidance and support throughout my research. I'm also grateful to Professor Yoshihiko Hirai and Professor Seiji Akita for their useful advice and reviewing this thesis.

I am indebted to Professor Atsushi Ashida and assistant professor Daisuke Kiriya for their invaluable suggestion from very beginning of my research. Especially I am deeply grateful to associate professor Takeshi Yoshimura for coordinating and supporting my research. I also would like to thank Dr. Syuichi Murakami for his generous support for fabricating MEMS structure.

I would like to acknowledge Dr. Katsuya Ujimoto, Mr. Yusaku Kawahara, Mr. Keisuke Wakazono, Mr. Yoshiki Yachi, Dr. Yusuke Miyata, Mr. Masaaki Aramaki, Mr. Ryota Kakihara, Takeru Douan, Mr. Kyohei Izumi, and all of my colleagues in Physics of Novel Devices Research group.

This work was supported by JSPS KAKENHI Grant Number 15J12596.

Finally, many thanks go to my parents.

Kento Kariya

February 2018

Original Articles Regarding This Thesis

No.	Title	Author	Journal	Related chapter
1	Piezoelectric properties of (100) orientated $BiFeO_3$ thin films on $LaNiO_3$	K. Kariya T. Yoshimura S. Murakami N. Fujimura	Japanese Journal of Applied Physics, vol. 53, No. 8S3, pp. 08NB02-1–08NB02-5 (2014).	Chapter 2
2	Enhancement of piezoelectric properties of (100)-orientated $BiFeO_3$ films on (100) $LaNiO_3$/Si	K. Kariya T. Yoshimura S. Murakami N. Fujimura	Japanese Journal of Applied Physics, vol. 53, No. 9S, pp. 09PA14-1–09PA14-4 (2014).	Chapter 2
3	Piezoelectric Vibrational Energy Harvester Using Lead-Free Ferroelectric $BiFeO_3$ Films	T. Yoshimura S. Murakami K. Wakazono K. Kariya N. Fujimura	Applied Physics Express, vol. 6, No. 5, pp. 051501-1–051501-4 (2013).	Chapter 3
4	Development of Piezoelectric MEMS Vibration Energy Harvester Using (100) Oriented $BiFeO_3$ Ferroelectric Film	S. Murakami T. Yoshimura K. Satoh K. Wakazono K. Kariya N. Fujimura	Journal of Physics: Conference Series, vol. 476, 012007, 5 pages, (2013).	Chapter 3

5	Output power of piezoelectric MEMS vibration energy harvesters under random oscillations	K. Kariya T. Yoshimura S. Murakami N. Fujimura	Journal of Physics: Conference Series, vol. 557, 012101, 5 pages, (2014).	Chapter 3
6	Quantitative analysis of direct piezoelectric response for $BiFeO_3$ films by scanning probe microscopy	K. Kariya T. Yoshimura K. Ujimoto N. Fujimura	Nature Materials, submitted.	Chapter 4

Other Articles Regarding This Thesis

No.	Article	Author	Journal
1	Enhancement of Direct Piezoelectric Properties of Domain-Engineered(100)BiFeO$_3$ Films	T. Yshimura K. Ujimoto Y. Kawahara K. Wakazono K. Kariya N. Fujimura S. Murakami	Japanese Journal of Applied Physics, vol. 52, No. 9S1, pp. 09KA03-1–09KA03-4 (2013).
2	Thickness dependence of piezoelectric properties of BiFeO$_3$ films fabricated using rf magnetron sputtering system	M. Aramaki K. Kariya T. Yoshimura S. Murakami N. Fujimura	Japanese Journal of Applied Physics, vol. 55, No. 10S, pp. 10TA16-1–10TA16-5 (2016).
3	Investigation of piezoelectric energy harvesting from human walking	R. Kakihara K. Kariya Y. Matsushita T. Yoshimura N. Fujimura	Journal of Physics: Conference Series, accepted